

Sea Ice Enhancements to Polar WRF*

KEITH M. HINES

Polar Meteorology Group, Byrd Polar and Climate Research Center, The Ohio State University, Columbus, Ohio

DAVID H. BROMWICH

*Polar Meteorology Group, Byrd Polar and Climate Research Center, and Atmospheric Sciences Program,
Department of Geography, The Ohio State University, Columbus, Ohio*

LESHENG BAI

Polar Meteorology Group, Byrd Polar and Climate Research Center, The Ohio State University, Columbus, Ohio

CECILIA M. BITZ

Department of Atmospheric Sciences, University of Washington, Seattle, Washington

JORDAN G. POWERS AND KEVIN W. MANNING

National Center for Atmospheric Research, Boulder, Colorado

(Manuscript received 16 October 2014, in final form 17 February 2015)

ABSTRACT

The Polar Weather Research and Forecasting Model (Polar WRF), a polar-optimized version of the WRF Model, is developed and made available to the community by Ohio State University's Polar Meteorology Group (PMG) as a code supplement to the WRF release from the National Center for Atmospheric Research (NCAR). While annual NCAR official releases contain polar modifications, the PMG provides very recent updates to users. PMG supplement versions up to WRF version 3.4 include modified Noah land surface model sea ice representation, allowing the specification of variable sea ice thickness and snow depth over sea ice rather than the default 3-m thickness and 0.05-m snow depth. Starting with WRF V3.5, these options are implemented by NCAR into the standard WRF release. Gridded distributions of Arctic ice thickness and snow depth over sea ice have recently become available. Their impacts are tested with PMG's WRF V3.5-based Polar WRF in two case studies. First, 20-km-resolution model results for January 1998 are compared with observations during the Surface Heat Budget of the Arctic Ocean project. Polar WRF using analyzed thickness and snow depth fields appears to simulate January 1998 slightly better than WRF without polar settings selected. Sensitivity tests show that the simulated impacts of realistic variability in sea ice thickness and snow depth on near-surface temperature is several degrees. The 40-km resolution simulations of a second case study covering Europe and the Arctic Ocean demonstrate remote impacts of Arctic sea ice thickness on midlatitude synoptic meteorology that develop within 2 weeks during a winter 2012 blocking event.

* Byrd Polar Research Center Contribution Number 1534.

Corresponding author address: Keith M. Hines, Polar Meteorology Group, Byrd Polar and Climate Research Center, The Ohio State University, 1090 Carmack Rd., Columbus, OH 43210-1002.
E-mail: hines.91@osu.edu

1. Introduction

Sea ice, which provides a layer of thermal insulation between the ocean and atmosphere and reflects most of the incident solar insolation, is central to polar climate studies (e.g., Vihma 2014). During the twentieth century, Southern Hemisphere sea ice was characterized by

large seasonal variations in areal coverage of relatively thin ice surrounding the Antarctic continent, while much of the Northern Hemisphere's sea ice was thicker multiyear ice in the Arctic Ocean that was closer to the pole and surrounded by landmasses. The twenty-first century, however, has seen dramatic changes in Arctic sea ice, especially a large reduction in summer sea ice extent (e.g., [Stroeve et al. 2007, 2012](#); [Comiso et al. 2008](#); [Screen et al. 2011](#)). Correspondingly, the volume of Arctic multiyear ice is decreasing with more of the ice pack composed of thinner seasonal sea ice and with impacts on the surface energy balance ([Deser et al. 2010](#); [Kwok and Untersteiner 2011](#); [Porter et al. 2011](#); [Persson 2012](#); [Semmler et al. 2012](#); [Hudson et al. 2013](#)). Both the cause and consequences of the ice loss are linked to the sea ice albedo feedback and radiative greenhouse gas forcing ([Serreze et al. 2007](#); [Comiso et al. 2008](#); [Kay et al. 2011](#); [Jaiser et al. 2012](#)). This has prompted considerable discussion of the role of sea ice in Arctic amplification (e.g., [Serreze and Francis 2006](#); [Serreze et al. 2009](#); [Screen and Simmonds 2010](#); [Screen et al. 2012](#)). In contrast, Antarctic sea ice extent has increased. [Simmonds \(2015\)](#) found the positive Antarctic trend for 1978–2013 is 28% of the magnitude of the Arctic negative trend. Large regional increases and decreases in sea ice extent, however, are apparent in the Southern Ocean and the latter contribute to rapid warming observed on the western Antarctic Peninsula (e.g., [Stammerjohn et al. 2008](#)).

Numerous studies have shown the impact of open water fraction on Northern and Southern Hemisphere climate (e.g., [Simmonds and Budd 1991](#); [Simmonds and Wu 1993](#); [Murray and Simmonds 1995](#); [Alexander et al. 2004](#); [Magnusdottir et al. 2004](#); [Rinke et al. 2006](#); [Singarayer et al. 2006](#); [Honda et al. 2009](#); [Seierstad and Bader 2009](#); [Serreze et al. 2009](#); [Deser et al. 2010](#); [Petoukhov and Semenov 2010](#); [Porter et al. 2012](#); [Semmler et al. 2012](#); [Strey et al. 2010](#); [Yang and Christensen 2012](#); [Screen et al. 2013](#); [Cassano et al. 2014](#); [Screen et al. 2014](#)). The characteristic local response, where open water fraction is increased or sea ice is removed, is an increase in winter temperature, lower-tropospheric thickness, and sensible heat flux, while the sea level pressure decreases ([Vihma 2014](#)). As open water fraction is increased, the local response is monotonic and usually nonlinear (e.g., [Ledley 1988](#)). In a simulation with a large-scale climate model, [Murray and Simmonds \(1995\)](#) found nearly half the impact of complete Arctic ice removal was achieved with the specification of 20% open water fraction. The early modeling study of [Royer et al. \(1990\)](#) showed that removal of Arctic sea ice produces compensating increases in sea level pressure elsewhere and reduces the strength of the

tropospheric polar vortex. Warming was not uniform in the Northern Hemisphere extratropics; instead, they found statistically significant cooling for a few locations over Arctic land. Many atmospheric numerical modeling studies since [Royer et al.](#) have explored the nonlocal impacts of specified Arctic sea ice extent. These studies show considerable variability in how they specify the forcing and in their results, but they emphasize significant nonlocal modulation (e.g., [Francis et al. 2009](#)).

Sensitivity to open water fraction is not evaluated in the present study. Rather, we introduce sea ice thickness and snow depth specifications for the Weather Research and Forecasting (WRF) Model ([Skamarock et al. 2008](#)). The local boundary layer role of sea ice thickness and snow depth on the atmosphere is shown, while an example of the nonlocal sensitivity to Arctic sea ice thickness and snow depth is explored. Similar to sea ice fraction, ice thickness and depth of overlying snow cover modulate the heat transfer between the ocean and atmosphere ([Ledley 1993](#); [Rinke et al. 2006](#); [Francis et al. 2009](#)). [Serreze et al. \(2009\)](#) find that the impact of sea ice thickness change is considerably less than that of sea ice extent change. Nevertheless, given that average Arctic sea ice thickness is decreasing in recent decades, it serves to enhance the effects of reduced sea ice coverage (e.g., [Lindsay et al. 2009](#); [Deser et al. 2010](#); [Laxon et al. 2013](#)). In a regional modeling study, [Rinke et al. \(2006\)](#) found better agreement between ERA-40 reanalysis fields and simulation results by setting a realistic sea ice thickness distribution rather than using uniform 2-m-thick sea ice.

The next section discusses new datasets for sea ice thickness and snow depth. [Section 3](#) details the numerical model. [Section 4](#) describes the western Arctic domain, sea ice conditions during January 1998, and observations used for comparison with model results. Results of the January 1998 simulations are shown in [section 5](#). The winter 2012 simulations are described in [section 6](#), and the results are shown in [section 7](#). Finally, conclusions are stated in [section 8](#).

2. New datasets for sea ice thickness and snow depth over sea ice

Beyond the changes in sea ice concentration well documented by decades of satellite remote sensing, the available submarine and ICESat observations show reduced sea ice thickness in the Arctic ([Kwok and Rothrock 2009](#)). Detailed spatial and temporal records of polar sea ice thickness, however, have been lacking during most of the modern satellite era. Fortunately, new thickness datasets are becoming available based upon satellite observations (e.g., [Kwok et al. 2009](#)) and modeling studies (e.g., [Lindsay et al. 2009](#)). The former

are sensitive to input values for sea ice density and snow depth over the sea ice, and uncertainties in Arctic ice thickness are estimated at 0.28 m in late winter and 0.21 m in fall (Zygmuntowska et al. 2014). Uncertainties in ICESat-based thickness estimates are larger in the Southern Hemisphere. Kern and Spreen (2015) estimate the uncertainty is about 0.7 m for the Weddell Sea.

The very recent Arctic System Reanalysis (ASR) covering 2000–12 sought gridded, high-resolution thickness distributions with input from passive remote sensing (Bromwich et al. 2010). The University of Illinois, in conjunction with the National Snow and Ice Data Center (NSIDC), were able to achieve this goal by first estimating sea ice age, which was then converted into sea ice thickness, through the allowance for typical annual cycles (e.g., Maslanik et al. 2007, 2011). In particular, new Arctic sea ice thickness distributions at 6.25-km horizontal resolution were produced for summers from 2002 to 2011 with input from Advanced Microwave Scanning Radiometer–Earth Observing System (AMSR-E) observations. The sea ice thickness values for 2000 to summer 2002 and after 2011 were produced at 25-km resolution based upon alternative satellite remote sensing products.

Other efforts have also produced gridded sea ice thickness distributions for recent decades. For instance, a data assimilation with an ice and ocean model, known as the Pan-Arctic Ice Ocean Modeling and Assimilation System (PIOMAS; Lindsay et al. 2009; Schweiger et al. 2011; Laxon et al. 2013), has been used to estimate sea ice thickness at approximately 25-km resolution. PIOMAS used the National Centers for Environmental Prediction–National Center for Atmospheric Research (NCEP–NCAR) reanalysis dataset for the atmospheric forcing. The ice thickness estimates have a mean difference of less than 0.1 m from ICESat thickness estimates adjacent to submarine observations (Schweiger et al. 2011). The error, however, is larger where those observations are not available. Sea ice thickness estimates derived from *CryoSat-2* observations display similar patterns to those of PIOMAS during the winter of 2011/12 (Laxon et al. 2013). PIOMAS produced slightly thinner winter sea ice than the derivation from *CryoSat-2*, but had similar summer thickness.

The spatial and temporal distribution of snow depth over sea ice also represented a data void until very recently, similar to ice thickness. Ledley (1993) studied the impact of snow on sea ice and discussed how it cooled the climate system, increased albedo, and decreased turbulent energy transfer. A gridded, time-dependent dataset is now available, as the PIOMAS project combined satellite observations with model

simulations to estimate distributions of snow depth over Arctic sea ice.

3. Polar WRF

Simulations are conducted with the polar-optimized version of WRF version 3.5 (V3.5) known as Polar WRF (<http://polarmet.mps.ohio-state.edu/PolarMet/pwrf.html>). Mesoscale simulations with WRF have generally used simple representations for sea ice thickness and snow depth on sea ice. WRF's Noah land surface model (LSM) for versions up to V3.4.1 specifies a sea ice thickness of 3 m (Chen and Dudhia 2001). Processes including snowfall and frost can increase the snow depth over sea ice. In the standard Noah scheme, however, if the water equivalent depth of snow falls below 0.01 m, it is reset to 0.01 m, and the snow depth is reset to 0.05 m. Previously, constant sea ice thickness and constrained snow depth were not unreasonable approximations given that most atmospheric mesoscale model users did not have access to temporal and spatial observations required for more precise specifications. Coupled models can predict ice thickness, but come with added burdens such that most mesoscale applications still use atmospheric models with specified surface conditions. Consequently, better sea ice surface specifications are needed for atmospheric simulations. With improved gridded datasets for sea ice and snow now becoming available, the WRF sea ice specification can be improved.

Polar optimizations are primarily within the Noah LSM and improve the representation of heat transfer through snow and ice. Fractional sea ice was implemented in Polar WRF by Bromwich et al. (2009) and has been an option in the standard release beginning with V3.1. More recently, WRF Noah was modularized starting with the standard release of V3.4 through the creation of separate modules for glacier-free land, land ice (e.g., glacier), and sea ice grid points. Key components for the standard release WRF V3.5 include options allowing users to specify spatially varying sea ice thickness and snow depth on sea ice. These updated options were developed by the Polar Meteorology Group (PMG) at Ohio State University's Byrd Polar and Climate Research Center for the ASR starting with Polar WRF version 3.1.1. The more general implementation was accomplished with the help of the Mesoscale and Microscale Meteorology Division at NCAR that partners with Ohio State University on the ASR and Antarctic Mesoscale Prediction System (AMPS; Powers et al. 2012). See the appendix for more details on the sea ice modifications. Other options allow an alternate calculation of surface temperature over

snow surfaces or setting the thermal diffusivity of the top 0.1-m-deep tundra soil to $0.25 \text{ W m}^{-1} \text{ K}^{-1}$, representative of highly organic soil. Alternative specifications of sea ice albedo are also included (e.g., Bromwich et al. 2009; Wilson et al. 2011).

The choice of physical parameterizations for the simulations described here is based upon the previous history of Polar WRF usage (e.g., Bromwich et al. 2009; Hines et al. 2011; Wilson et al. 2011, 2012; Steinhoff et al. 2013). The Grell–Freitas scheme (Grell and Freitas 2013) is used for cumulus parameterization, and the two-moment Morrison scheme (Morrison et al. 2005) is applied for cloud microphysics. For the atmospheric boundary layer and the corresponding atmospheric surface layer we use the Mellor–Yamada–Nakanishi–Niino (MYNN; Nakanishi and Niino 2006) level-2.5 scheme. We use the climate-model-ready update to the Rapid Radiative Transfer Model, known as RRTMG (Clough et al. 2005), for longwave and shortwave radiation, as recent testing indicates improved radiative fields. Fractional sea ice concentrations for the Noah LSM are taken from the 25-km resolution bootstrap algorithm for *Nimbus-7* SMMR and DMSP SSM/I–SSMIS observations (Comiso 2000).

We select Arctic winter cases when the temperature difference between the bottom of the sea ice and the overlying atmosphere is large. This is an appropriate time of the year to test the options for thickness of sea ice, and snow depth on sea ice, which are turned on and based upon daily PIOMAS estimates at approximately 25-km horizontal resolution, unless the values are otherwise prescribed. The University of Washington provides the PIOMAS distributions of thickness and snow depth for sea ice, which are ingested into WRF through the WRF Preprocessing System (WPS). Minimum (maximum) specifications are set at 0.1 (10) m for sea ice thickness and 0.001 (1) m for snow depth. Since the simulation periods are prior to the onset of spring snow melting over sea ice, sea ice albedo is specified at 0.82. Summer simulations should use smaller albedos; alternative albedo options are available in Polar WRF.

Other specifications include 39 terrain-following η levels in the vertical dimension, reaching from the earth's surface to 10 hPa, with the lowest layer centered at 11 m AGL. The model is run in forecast mode with a series of 48-h segments initialized daily at 0000 UTC. Earlier idealized mesoscale simulations for Antarctica by Parish and Waight (1987) found large boundary layer adjustments in the first 10 h, while Hines and Bromwich (2008) found very little difference in their results between 12- and 24-h spinup times for Polar WRF over Greenland. We select 24-h spinup of the hydrologic cycle and the boundary layer similar to Hines et al. (2011)

and Wilson et al. (2011) to provide a firm test and ensure adequate adjustment. Accordingly, near-surface values will adjust to the model's surface energy balance and may differ from the initial conditions. Output beginning at hour 24 of the most recent segment is spliced into a record of the simulated period. Furthermore, specified initial and boundary conditions for the atmospheric fields are taken from the ERA-Interim (ERA-I; Dee et al. 2011) fields available every 6 h on 32 pressure levels and with the surface at T255 resolution.

Cassano et al. (2011) and Glisan et al. (2013) show that inclusion of spectral nudging, a scale-dependent damping toward a prescribed pattern, is effective at reducing the gradual drift toward unrealistic seasonal flow patterns over the Arctic. Finer-scale features are determined by the mesoscale model. Berg et al. (2013) find that spectral nudging had minimal direct impact on the surface energy balance. Consequently, we will still see the local impact of sea ice changes. Therefore, spectral nudging with truncation at wavenumber 6 in both horizontal directions is applied in case study 1 to the atmosphere above model level 10 (approximately 900 hPa over the Arctic Ocean) to limit biases from developing in the large-scale pressure and wind fields. The nudging is applied to the temperature, geopotential, and u - and v -wind components with ERA-I fields at 6-h intervals as the basis for the large-scale forcing.

Polar WRF has been tested over permanent ice (Hines and Bromwich 2008; Bromwich et al. 2013), Arctic pack ice (Bromwich et al. 2009), and Arctic land (Hines et al. 2011; Wilson et al. 2011, 2012). The model has been applied to various polar applications including Antarctic real-time weather forecasts (e.g., Powers et al. 2012).

4. Case study 1: Arctic domains and sea ice conditions

The first set of WRF simulations presented here are on a 250×250 polar stereographic grid centered at the North Pole and extending to 59°N at the corners (Fig. 1). The horizontal grid spacing is 20 km. The grid includes the entire Arctic Ocean and a large majority of the Northern Hemisphere sea ice domain. The January location of the ice station for the Surface Heat Budget of the Arctic Ocean project (SHEBA; Uttal et al. 2002) is marked in Fig. 1. WRF results are bilinearly interpolated to concurrent locations of the drifting ice station for comparison to the SHEBA observed surface data, analogous to the procedure in Bromwich et al. (2009). The only high-resolution forcing near SHEBA is by the sea ice fields.

We select January 1998 as a period of study, as mid-winter is a time of maximum contrast between liquid

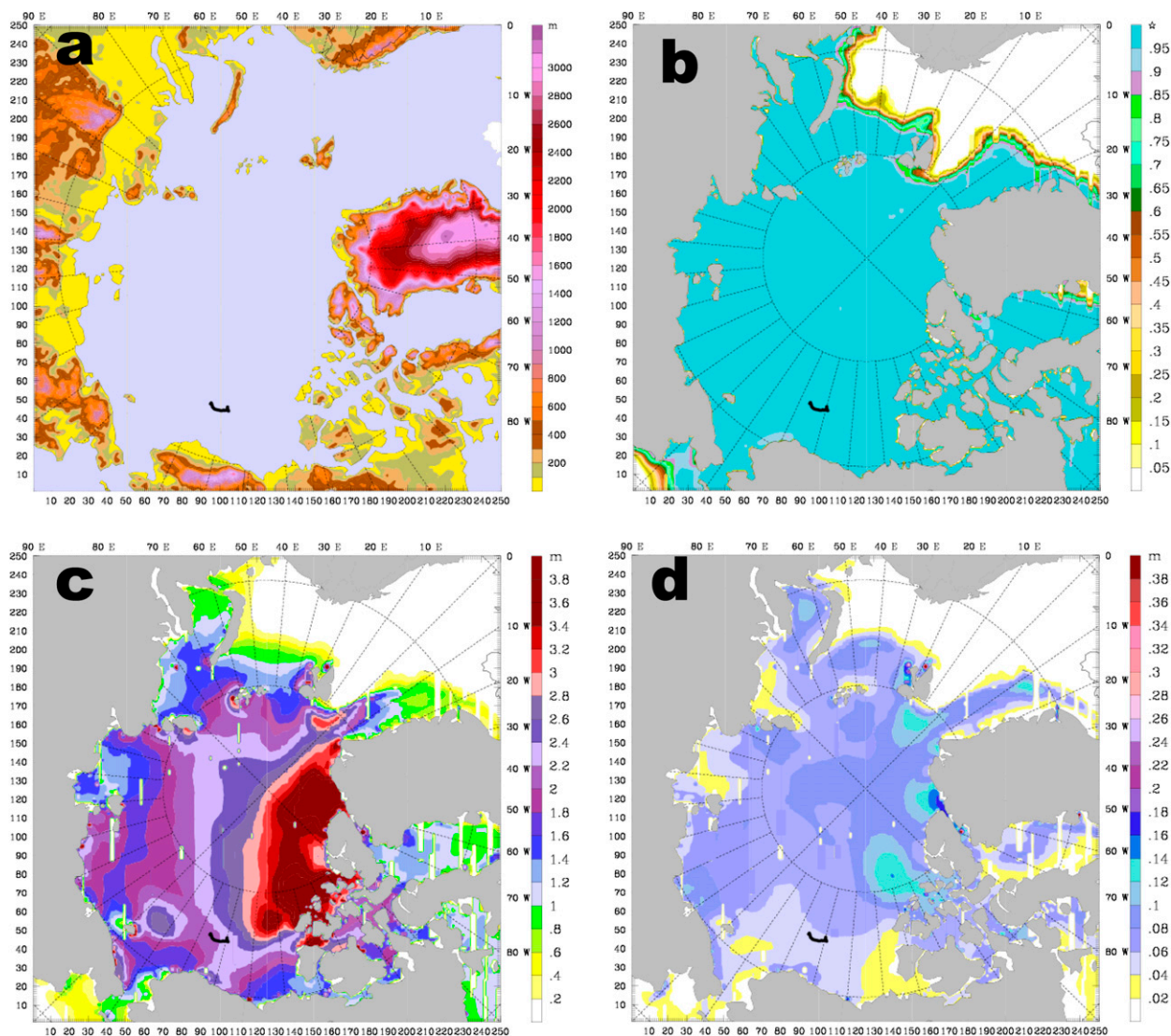


FIG. 1. Map of Arctic domain showing average January 1998 values of (a) topography (m), (b) sea ice concentration (fraction), (c) sea ice thickness (m), and (d) snow depth on sea ice (m). The January 1998 location of ice station SHEBA is marked by the thick black curve.

ocean temperature (approximately -1.8°C adjacent to sea ice) and near-surface atmospheric temperature over the Arctic Ocean. Very little sunlight falls on the Arctic Ocean during January, so the radiative forcing in the heart of the domain is essentially due to longwave processes. Furthermore, ice station SHEBA observations are used for comparison because of the unprecedented quantity and quality of data provided by the 13-month-long (1997–98) field campaign (Perovich et al. 1999; Persson et al. 2002). Among the SHEBA observations are latitude, longitude, surface pressure, temperature, velocity, humidity, turbulent fluxes, and radiative fluxes (Persson et al. 2002). Quality controlled values can found online ([ftp://ftp.etl.noaa.gov/users/opersson/sheba/](http://ftp.etl.noaa.gov/users/opersson/sheba/)).

Average January 1998 sea ice features are displayed in Fig. 1. A series of thirty-two 48-h segments were simulated first with unmodified WRF specified with variable sea ice fraction, 3-m-thick sea ice, and 0.05-m snow depth on sea ice. The ice thickness and snow depth on sea ice are the previous default Noah settings in WRF. This first simulation listed in Table 1 is referred to as standard WRF 3.5. January 1998 is then simulated with Polar WRF using prescribed, spatially varying conditions for the concentration, thickness, and snow depth of the sea ice. The Polar WRF 3.5 simulation is the second simulation listed in Table 1. The 48-h segments first begin at 0000 UTC 31 December 1997, with the last one ending at 0000 UTC 2 February 1998. Only output

TABLE 1. Numerical simulations with WRF 3.5 for January 1998.

Simulation	Model version	Sea ice thickness (m)	Snow depth (m)	Ensemble
Simulations for 31 Dec 1997–1 Feb 1998				
Standard	Standard WRF 3.5	3	0.05	1
Polar WRF	Polar WRF 3.5	Variable	Variable	1
Simulations for 15–26 Jan 1998				
1mSeaice	Polar WRF 3.5	1	Variable	5
2mSeaice	Polar WRF 3.5	2	Variable	5
3mSeaice	Polar WRF 3.5	3	Variable	5
2cmSnow	Polar WRF 3.5	Variable	0.02	5
5cmSnow	Polar WRF 3.5	Variable	0.05	5
10cmSnow	Polar WRF 3.5	Variable	0.10	5
25cmSnow	Polar WRF 3.5	Variable	0.25	5

values during January are included in the calculated statistics. Averages are calculated for grid points with greater than 50% sea ice fraction over the Arctic as a whole, and for specific latitude ranges to check if the results at SHEBA are typical of Arctic sea ice. Figure 1b shows that the January sea ice concentration is greater than 95% at nearly all sea ice points, except for those grid points in the marginal ice zone. North of 80°N, more than 98% of the Arctic Ocean is covered by sea ice for most of January (Fig. 2a). There is a substantial amount of open water in the North Atlantic south of 75°N, with a tongue of open water extending west of Svalbard to 80°N.

Figure 1c shows the average sea ice thickness for January 1998 as obtained from the PIOMAS analysis. Average thickness varies from less than 0.4 m in the Bering Sea and locations in the North Atlantic to greater than 3.5 m north of Greenland and eastern Canada. Arctic average PIOMAS thickness is about 1.91 m during January 1998 (Table 2). During January, the PIOMAS thickness of sea ice increases both at SHEBA

and over the Arctic domain as a whole, with the thickness typically 0.25 m larger at SHEBA than the Arctic average (Fig. 2b). Given this slight difference, we take the thickness at SHEBA to be a representative value for the Arctic.

PIOMAS snow depth over sea ice generally increases with increasing latitude, with some locations on the edge of the sea ice domain having less than 0.04 m and about 0.1 m near the North Pole (Fig. 1d). Isolated pockets adjacent to land have up to 0.2-m snow depth. Table 2 provides statistics for the snow depth. In contrast, climatological estimates of snow depth compiled by Warren et al. (1999) based upon 1954–91 Soviet drifting station observations on Arctic multiyear ice would suggest January snow depths greater than 0.2 m are widespread for the Arctic Ocean. The sea ice thickness in the Arctic Ocean increases northward toward the North Pole with the average thickness being 2.88 m north of 85°N (Table 2). Average snow depth also tends to increase toward the North Pole. Thus, it is 0.087 m deep north of 80°N, yet 0.066 m deep over the Arctic sea

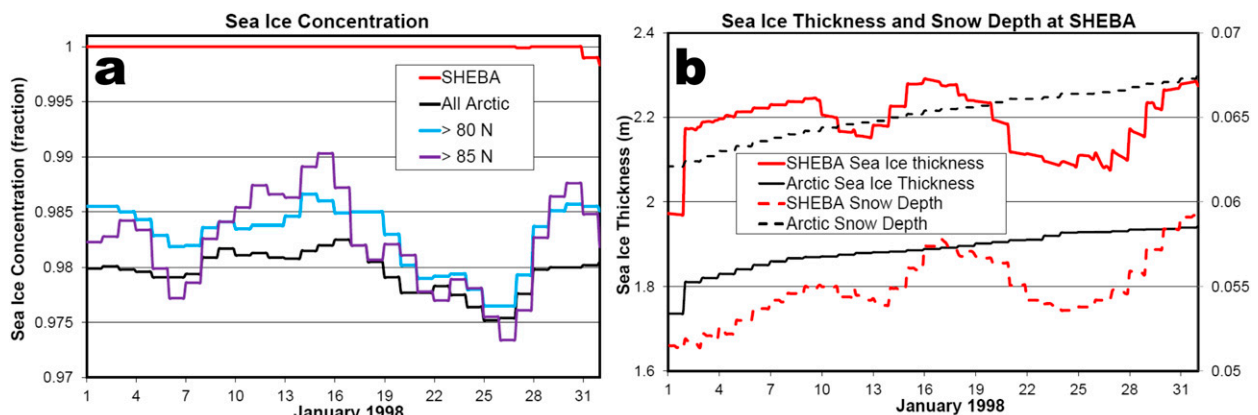


FIG. 2. Time series of (a) sea ice concentration (fraction) and (b) sea ice thickness (m) and snow depth on sea ice (m) for January 1998 for ice station SHEBA (red lines) and all Arctic sea ice grid points (black lines). The blue and purple lines in (a) represent areas north of 80° and 85°N, respectively. The right scale in (b) is snow depth (m).

TABLE 2. January 1998 sea ice averages for ice station SHEBA and grid points with sea ice concentrations greater than 0.5.

Location	Sea ice concentration	PIOMAS sea ice thickness (m)	PIOMAS snow depth (m)
SHEBA	1.000	2.16	0.055
Sea ice points in domain	0.978	1.91	0.066
Sea ice points north of 85°N	0.979	2.88	0.087
Sea ice points north of 80°N	0.980	2.63	0.087
Sea ice points north of 75°N	0.981	2.29	0.078
Sea ice points north of 70°N	0.980	2.04	0.070
Standard WRF Noah settings	Variable	3.00	0.05

ice as a whole. The PIOMAS average for SHEBA, 0.055 m, is slightly less than the monthly average for all Arctic sea ice (Fig. 2b). This value is not in good agreement with the in situ snow observations at SHEBA that show typical depth being slightly more than 0.2 m during January. Nevertheless, given that the PIOMAS differences from the Arctic means are small at SHEBA, with slightly more insulation due to somewhat thicker ice and slightly less insulation due to slightly smaller snow depth, the heat transfer through snow and ice there should be reasonably representative of the Arctic Ocean, based upon PIOMAS values during January 1998. Furthermore, the standard WRF Noah LSM value of 0.05-m snow depth may be reasonable for January 1998. The standard ice thickness setting of 3 m, however, is too large in comparison to the January 1998 PIOMAS analysis.

5. Results of case study 1

Figure 3 shows time series of meteorological fields for SHEBA observations and the standard and Polar WRF simulations. State variables for ERA-I are also shown. WRF results at SHEBA are basically consistent with the earlier Bromwich et al. (2009) study that ran Polar WRF V2.2 with a western Arctic domain. Table 3 shows selected simulation performance statistics for temperature, surface pressure, humidity, wind speed, and surface fluxes. WRF performance is quite good with correlations of 0.79 or better for all fields shown except the surface turbulent flux fields. Performance of the standard WRF V3.5 and Polar WRF V3.5 are very similar, with the latter having lower root-mean-square errors for all fields except for 10-m wind speed and the surface turbulent fluxes. Since the ERA-I values are from a reanalysis, not a forecast of at least 24 h, they are superior to those of WRF for the surface pressure and the 2-m temperature. ERA-I assimilates skin temperature differently than 2-m temperature; consequently, the skin temperature bias is 2.1 K, while its 2-m temperature bias is 0.5 K. The differences between the ERA-I and WRF fields emphasize the impact of spinup in the near-surface fields.

The surface pressure time series (Fig. 3a) show that the standard WRF 3.5 and Polar WRF 3.5 simulations capture most of the synoptic pressure change during January. Events with increased longwave radiation, however, are undersimulated in both standard and Polar WRF experiments (Fig. 3f). These warm events are not properly represented in the temperature time series (Figs. 3c,d) and contribute to the overall cold bias. Bromwich et al. (2009) found similar errors in simulating the warm events on 3–5 and 10–11 January. We linked events with increased longwave radiation (Fig. 3f) to the presence of clouds. Time series of vertically integrated cloud water and cloud ice (not shown) were calculated. Most of the simulated cloud water substance during January was in medium-height ice clouds. Nontrivial amounts of simulated cloud water were found on 4, 7, 27, and 29 January, while nontrivial cloud ice was found on 2–3, 4, 7, 9–10, and 31 January. Additionally, varying amounts of cloud ice were present during 25–30 January. These cloudy periods match times of simulated incident longwave radiation greater than 180 W m^{-2} . Furthermore, thin medium and low clouds were present on late 8 January, and the event has a signature in Fig. 3f.

Cold events, when the incident longwave radiation is reduced, are better simulated (e.g., Bromwich et al. 2009). During the first half of the 13–25 January cold event, the standard WRF 3.5 simulated temperature is closer to the observed field. During the latter part, the Polar WRF 3.5 simulation is closer to the observations. The standard WRF run is slightly colder than the Polar WRF run, with differences being largest during cold events. Standard WRF 3.5 has an overall bias of -2.0°C for the skin temperature, while Polar WRF 3.5 has a bias of -0.8°C . For 2-m temperature, the biases are -2.5°C for standard WRF and -1.2°C for Polar WRF.

These biases suggest that the simulated near-surface static stability differs from that of the observed temperature profile. By partitioning into relatively cold and warm cases, we found that when the observed 2-m temperature was colder than -32°C (approximately

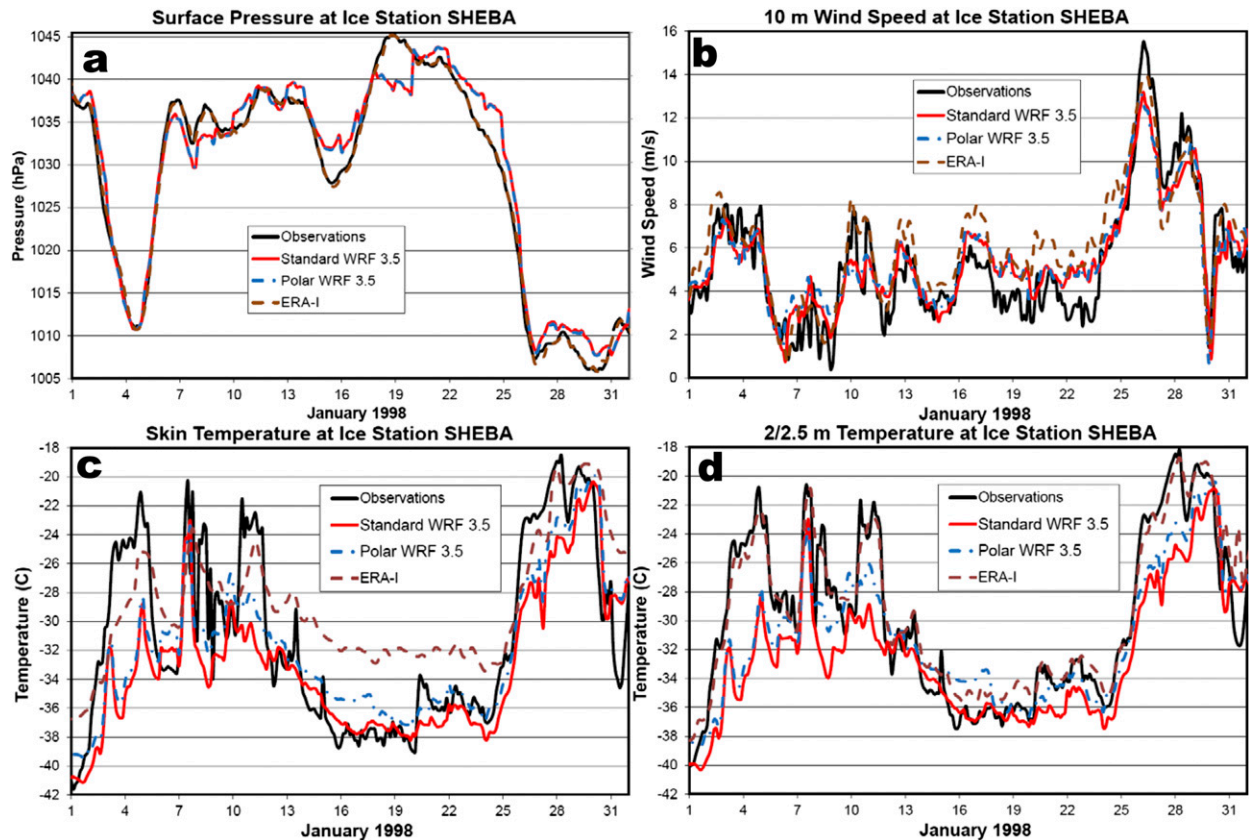


FIG. 3. Time series for January 1998 showing ice station SHEBA values of (a) surface pressure (hPa), (b) 10-m wind speed (m s^{-1}), (c) skin temperature ($^{\circ}\text{C}$), (d) 2.5-m (observed) and 2-m (simulated) temperature ($^{\circ}\text{C}$), (e) specific humidity (g kg^{-1}), (f) incident longwave radiation (W m^{-2}), (g) sensible heat flux (W m^{-2}), and (h) latent heat flux (W m^{-2}).

half of January), the average of the observed 2-m value was 1.5°C warmer than the skin value, while the difference was 0.9°C in the Polar WRF simulations. In contrast, when the observed temperature was warmer than -30°C , the difference was 0.6°C for averages of both observations and the Polar WRF simulation, as the inversion was weaker. Thus, the model appears to underrepresent the near-surface static stability under especially cold and stable conditions, which are associated with clear skies and strong inversions.

The slight positive bias in the wind speed (Fig. 3b) probably contributes to the excess magnitude of the (downward directed) sensible heat flux during the colder part of the month (Fig. 3g). This is most apparent when the simulated wind speed is larger than that observed near 17 January. Another contribution may come from the difficulty models have in simulating the very stable boundary layer denoted by the represented turbulent heat flux, which is frequently larger than observed heat flux estimates. The cold bias at the surface cannot be explained by the heat flux from the atmosphere to the surface (which contributes to surface warming); instead,

the cold bias is probably due to the negative bias in the incident longwave radiation, which has magnitudes of 15.7 and 14.4 W m^{-2} for standard WRF 3.5 and Polar WRF 3.5, respectively (Fig. 3f; Table 3). This error primarily occurs when cloud ice and/or cloud water are present. Nevertheless, WRF tends to simulate the surface fields near SHEBA well for most of the month of January. We will explore features that impact the surface energy balance below.

Figure 3 and Table 3 inspire us to test the contributions of sea ice thickness and snow depth on sea ice to the surface fields. Accordingly, new simulations are performed with either constant sea ice thickness or snow depth (Table 1). The sensitivity simulations are composed of a series of 51-h segments, beginning 0000 UTC 14 January and continuing until 0000 UTC 27 January. Simulations are initialized every 6 h to enable ensemble results beginning on 0000 UTC 16 January. Five member ensembles are used for statistical purposes. For every sixth hour of model output, results are taken from 24-, 30-, 36-, 42-, and 48-h forecasts available from different initialization times.

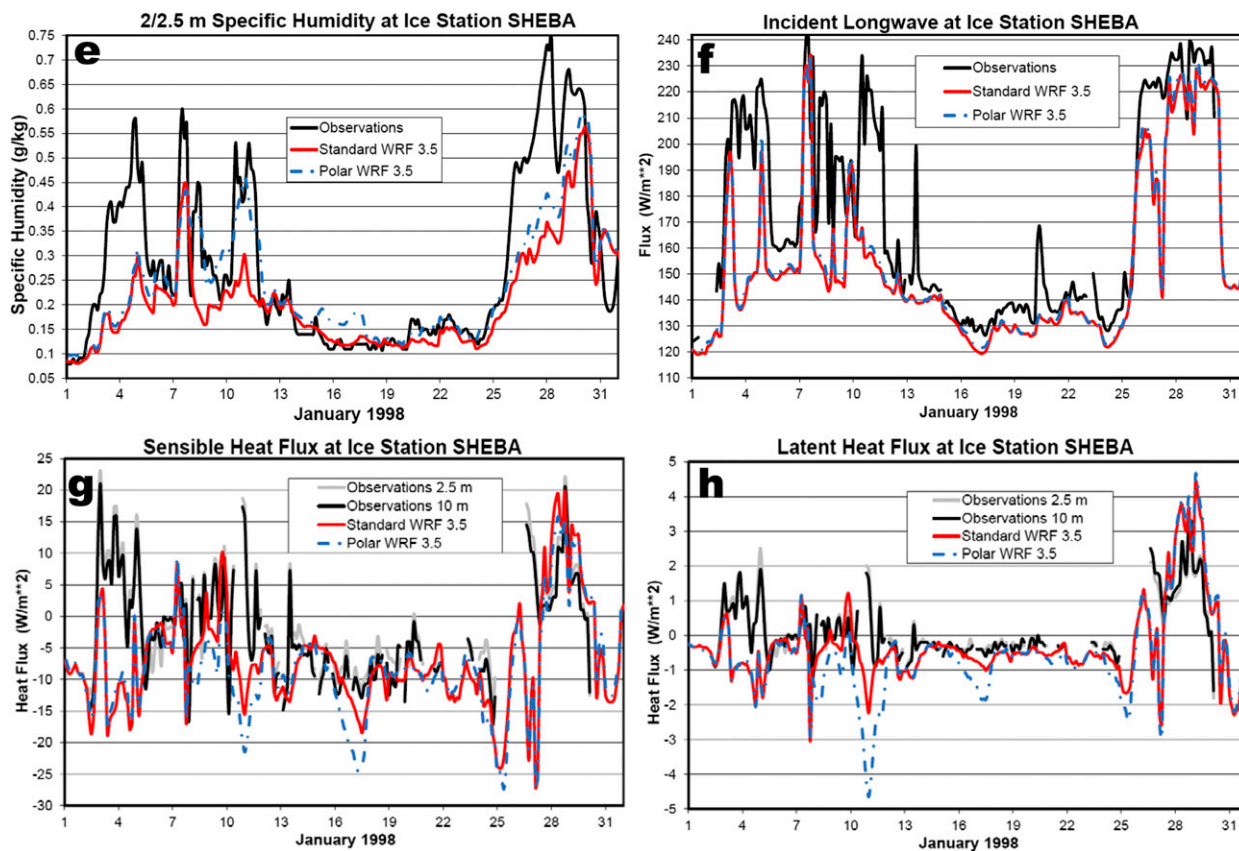


FIG. 3. (Continued)

At intermediate times, results are taken from 27-, 33-, 39-, 45-, and 51-h forecasts, so five-member results are available every 3 h. Displayed results show ensemble averages. The test period includes an extended cold, cloud-free event at SHEBA (Fig. 3), when upward heat flux through the sea ice should be important and sensitive to the specifications of ice thickness and snow depth. It also includes a change to cloudy conditions that begins by 25 January, so we can contrast how ice thickness and snow depth impact different radiative conditions. Snow depth over sea ice and ice thickness are otherwise the same as the Polar WRF 3.5 simulation except for the specifications listed here. To test sea ice thickness, three cases have constant time and space settings of either 3-, 2-, or 1-m-thick ice (see Table 1) at sea ice points. Furthermore, snow depth on sea ice is tested with four sensitivity cases using specified snow depths of either 0.02, 0.05, 0.10, or 0.25 m (Table 1). Snow depth in the 0.05-m case is roughly similar to that in the standard WRF 3.5 simulation. The 0.25-m case is within the range of realistic snow depths for the winter Arctic Ocean and only slightly larger than in situ observations at SHEBA.

Figure 4 and Table 4 show that results at SHEBA are sensitive to sea ice thickness and snow cover. The average skin (2 m) temperature in the Polar WRF 3.5 simulation at SHEBA is -34.8°C (-33.9°C) for the period from 0000 UTC 16 January to 0000 UTC 27 January. Those temperatures, however, are -32.8°C (-32.3°C) in the 1-m sea ice and -36.1°C (-35.3°C) in the 3-m sea ice experiments. For the average of all Arctic sea ice grid points, the temperature is somewhat warmer than at SHEBA, yet the difference in results between sea ice thickness experiments is similar. In the snow depth experiments, the SHEBA temperature varies between -34.2°C (-33.4°C) in the 0.02-m snow experiment and -38.3°C (-37.4°C) in the 25cmSnow case. Thus, the case-to-case temperature differences between sensitivity experiments can be as large as 5°C , which is larger than the near-surface temperature biases and similar in magnitude to the root-mean-square errors for standard WRF 3.5 and Polar WRF 3.5 simulations. The statistical significance of the ensemble differences at SHEBA was examined with a Student's *t* test. For variables shown in Table 4, all the differences between ensemble averages for specified

TABLE 3. January 1998 WRF 3.5 and Polar WRF 3.5 performance statistics compared to SHEBA observations.

Variable*	Correlation	Bias	RMSE
Surface pressure (hPa): 1029.0	0.98	0.7	2.5
	0.98	0.6	2.4
	1.00	-0.3	0.7
Skin temperature (°C): -31.1	0.81	-2.0	4.2
	0.83	-0.8	3.6
	0.84	2.1	4.1
2.5-/2-m temperature (°C): -29.9	0.85	-2.5	4.0
	0.86	-1.2	3.2
	0.97	0.5	1.6
10-m wind speed (m s ⁻¹): 5.3	0.92	0.1	1.2
	0.91	0.3	1.3
	0.89	0.9	1.6
2.5-/2-m specific humidity (g kg ⁻¹): 0.277	0.79	-0.070	0.129
	0.82	-0.034	0.105
Incident longwave radiation (W m ⁻²): 168.2	0.81	-15.7	26.6
	0.81	-14.4	25.7
Sensible heat flux (W m ⁻²): -2.9	0.33	-4.0	10.4
	0.33	-5.3	10.9
Latent heat flux (W m ⁻²): 0.1	0.52	-0.4	1.1
	0.48	-0.6	1.4

* Values directly next to the variable names are the observed averages at SHEBA. In the right three columns, the top values are for standard WRF 3.5 forecasts, the middle values are for Polar WRF 3.5 forecasts, and the bottom values, where available, are for ERA-I. WRF values are at 3-h intervals, while ERA-I values are at 6-h intervals. Observations for sensible and latent heat fluxes are based upon 10-m observations at SHEBA. Statistics based upon 2.5-m observations are similar.

constant sea ice thickness cases are statistically significant at the 1% confidence level. The differences between ensembles for cases of specified constant snow depth on sea ice are significant at the 1% confidence level, except for those of sensible heat flux.

The simulated sensitivities encourage us to represent ice thickness and snow depth as accurately as possible. Previously, [Seo and Yang \(2013\)](#) found a cold bias of several degrees in the marginal ice zone in a Polar WRF simulation with uniform 3-m-thick ice. They suggested more realistic, thinner sea ice would have helped. The 3-m-thick sea ice sensitivity case could approximately represent thicker ice conditions such as the region north of Greenland and northeastern Canada. The 1-m case is more representative of Antarctic sea ice or the Arctic marginal ice zone. Furthermore, the snow depth in 25cmSnow may be representative of the winter Arctic a few decades ago when multiyear ice was more extensive (e.g., [Warren et al. 1999](#)). Moreover, the near-surface temperature sensitivity displayed in [Fig. 4](#) demonstrates that changing the snow depth and ice thickness specifications can alter the sign of the temperature bias. The 1-m sea ice experiment is the warmest simulation, while the 0.25-m snow experiment is the coldest. Differences

are larger during the colder times of the test period and reduced during the warmer cloudy period starting near 25 January.

The temperature difference between sensitivity simulations is concentrated in the lowest levels of the model atmosphere ([Fig. 5](#)). Higher in the troposphere, the spectral nudging works to dampen out differences between simulations. Temperature differences between simulations are very small above the 100-m level. The temperature profile is nearly isothermal below level 2 (near 37 m) in 1mSeaice. Simulations 3mSeaice and 10cmSnow have very similar profiles, as do 2mSeaice and 5cmSnow.

If we consider the surface energy balance, the heat conduction flux in snow and ice (defined as positive for heat flow directed upward, i.e., in the direction from the ocean toward the interface with the atmosphere) is most obviously impacted by the sensitivity simulation specifications. The surface energy balance terms for sea ice grid points are

$$H \frac{\partial T_s}{\partial t} = \varepsilon[L(\downarrow) - \sigma T_s^4] + (1 - \alpha)S(\downarrow) - T_r - H_s - L_s + G + Q, \quad (1)$$

where H is the heat capacity of relevance to the skin temperature, t is time, ε is surface emissivity, $L(\downarrow)$ is downward longwave radiation, σ is the Stefan-Boltzmann constant, α is surface albedo, $S(\downarrow)$ is downward shortwave radiation, T_r is the shortwave radiation transmitted beyond the surface layer ([Persson 2012](#)), H_s is sensible heat flux, L_s is latent heat flux, G is heat conduction through ice and snow, and Q represents other diabatic processes including phase change and heat flux by precipitation. The Noah surface temperature, T_s , is computed diagnostically, rather than by a prognostic solution to [Eq. \(1\)](#). Sensible heat flux is frequently negative during winter as turbulence typically carries heat from the atmosphere to the earth's surface, where cooling is driven by upward net longwave radiative flux. The heat conduction term depends on the depth of snow and ice through which the heat flows. In the Noah LSM this term is inversely proportional to the sum of half the thickness of the upper ice layer (0.75 m thick in the standard WRF 3.5 simulation) and the depth of overlying snow. Thinner ice and reduced snow depth should increase the heat conduction for a fixed ocean-atmosphere temperature difference.

[Table 4](#) and [Fig. 6](#) demonstrate this relationship for the sensitivity tests. The greatest sensitivity occurs during cold periods when the incident longwave radiation is relatively small and the instantaneous heat conduction flux can exceed 50 W m⁻² in 1mSeaice, as the thin ice

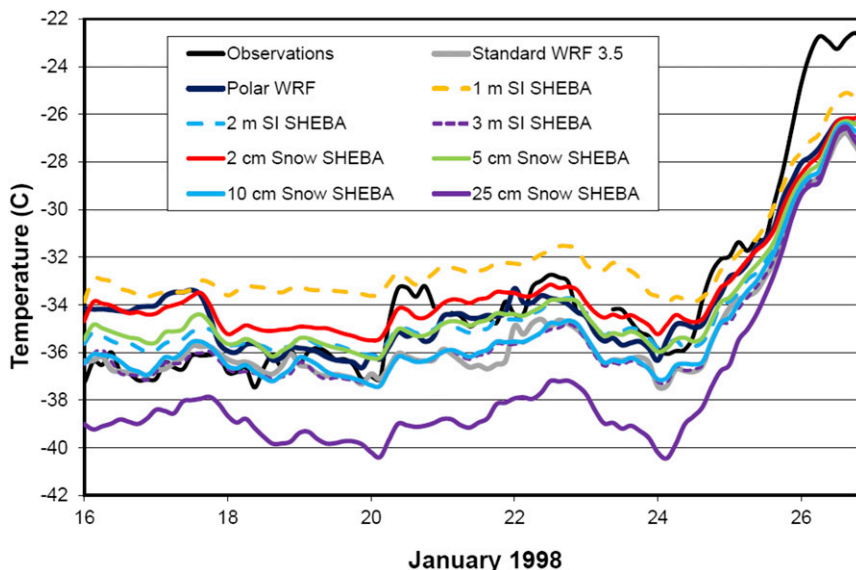


FIG. 4. Time series for 16–26 Jan 1998 showing ice station SHEBA values of 2.5-m (observed) and 2-m (simulated) temperature (°C). The observations are shown by the solid black line. Sea ice thickness sensitivity experiments are shown by the dashed color lines, and snow depth sensitivity experiments are shown by the solid color lines.

allows faster heat transfer. All curves approach 0, however, by 26 January when the normal upward heat flow is disrupted by a relatively warm synoptic event. The ice temperature in the top Noah layer and the skin temperature are similar at that time. The sensitivity of heat conduction flux within our prescribed experiments

is obvious from the time series. The flux varies at SHEBA by more than 12 W m^{-2} in the sea ice thickness experiments and more than 11 W m^{-2} in the snow depth experiments. The flux is 39% larger (3.5% smaller) in 1mSeaice (3mSeaice) than in Polar WRF 3.5. Therefore, there is greater sensitivity to decreased ice thickness than

TABLE 4. Averages from sensitivity test results for 16–26 Jan 1998. The first values are for the values at SHEBA. The second values are for the averages of all Arctic sea ice points with sea ice concentration greater than 0.5.

Simulation	Sea ice thickness (m)	Snow depth on sea ice (m)	Skin temperature (°C)	2-m temperature (°C)	Heat flux through ice (W m^{-2})	Sensible heat flux (W m^{-2})	Incident longwave radiation (W m^{-2})
Standard WRF 3.5	3	0.05	-36.0 -29.6	-35.2 -29.2	30.0 26.6	-11.0 -2.8	136.9 159.1
Polar WRF 3.5	Variable	Variable	-34.8 -27.6	-33.9 -27.9	31.3 44.6	-12.2 7.2	138.1 160.7
1mSeaice	1	Variable	-32.8 -29.9	-32.3 -29.3	43.5 42.9	-6.3 -8.8	138.8 142.8
2mSeaice	2	Variable	-35.0 -31.8	-34.2 -31.0	34.1 34.0	-9.6 -12.2	137.6 141.7
3mSeaice	3	Variable	-36.1 -32.8	-35.3 -31.9	30.2 30.2	-10.7 -13.3	137.0 141.3
2cmSnow	Variable	0.02	-34.2 -31.6	-33.4 -30.8	34.6 35.4	-10.7 -11.5	138.1 142.1
5cmSnow	Variable	0.05	-34.9 -32.2	-34.1 -31.3	33.0 34.7	-10.6 -12.7	137.6 141.7
10cmSnow	Variable	0.10	-35.9 -33.0	-35.1 -32.0	30.0 29.2	-11.1 -13.8	137.1 141.3
25cmSnow	Variable	0.25	-38.3 -35.0	-37.4 -33.8	23.1 22.2	-12.3 -15.6	136.1 140.4

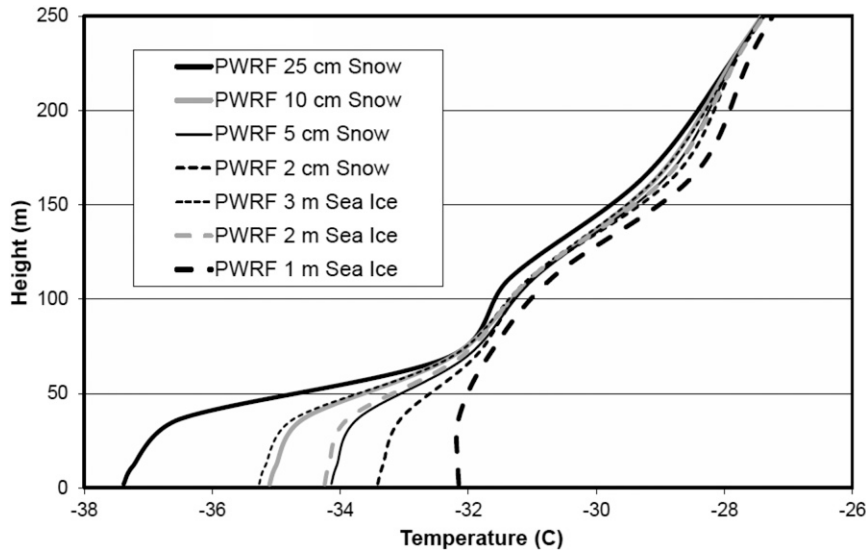


FIG. 5. Vertical profiles for 16–26 Jan 1998 showing ice station SHEBA values for temperature ($^{\circ}\text{C}$).

to increased thickness. In contrast, the largest relative change in heat flux due to snow depth occurs for 25cmSnow when the flux magnitude is reduced by 26% from Polar WRF 3.5. The insulation of sea ice by snow cover is readily apparent in 25cmSnow, which has a heat conduction flux 7–20 W m^{-2} smaller than the other snow depth experiments until 24 January. Table 4 demonstrates that these model results at SHEBA are similar to those of the Arctic sea ice average. The differences between ice thickness experiments are almost as large for the sea ice average as those at SHEBA. Moreover, the heat conduction flux differences

between snow depth experiments can be nearly 13 W m^{-2} for the sea ice average. Therefore, while the sensitivity amplitudes at SHEBA and the Arctic sea ice average vary somewhat, Table 4 indicates that results at SHEBA are qualitatively representative of the sensitivity to snow and ice specifications over Arctic sea ice.

As changing the ice thickness and snow depth change the surface energy balance, other terms in the balance can be indirectly impacted as Table 4 and Fig. 7 show. Sensible heat flux adjusts with other terms in Eq. (1) to form the surface energy balance. For 16–25 January,

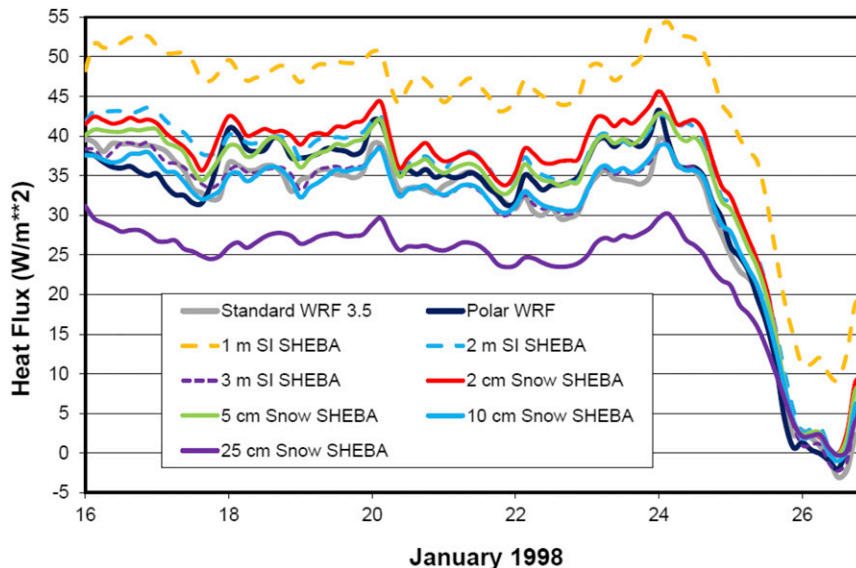


FIG. 6. Time series for 16–26 Jan 1998 showing ice station SHEBA values for ice heat flux (W m^{-2}). Sea ice thickness sensitivity experiments are shown by the dashed color lines, and snow depth sensitivity experiments are shown by the solid color lines.

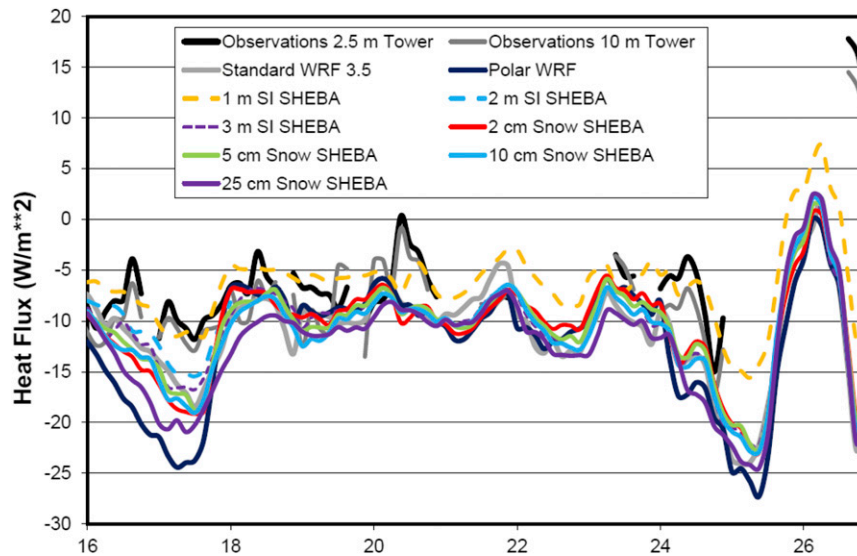


FIG. 7. Time series for 16–26 Jan 1998 showing ice station SHEBA values for sensible heat flux (W m^{-2}). Sea ice thickness sensitivity experiments are shown by the dashed color lines, and snow depth sensitivity experiments are shown by the solid color lines.

the sensible heat flux is typically negative (downward), with largest magnitude in colder experiments, partly compensating for reduced surface warming by heat conduction (Fig. 6). The percentage change in incident longwave radiation, however, is very small between experiments during this period (Table 4). Table 4 also indicates that surface energy balance terms at SHEBA respond similar to the general sensitivity to snow and ice specifications over Arctic sea ice.

6. Case study 2: Arctic, North Atlantic, and European grid

The previous section shows local impacts on the earth's surface and in the lower atmosphere on Arctic sea ice conditions. To demonstrate nonlocal impacts, we introduce a new 40-km grid (Fig. 8) that includes Europe, much of the North Atlantic and the Arctic Ocean, and portions of Asia and North America. Most of the sea ice in this domain is north of 80°N (Fig. 8b).

The selection of this grid is linked to recent interest in how Arctic sea ice loss impacts the climate in mid-latitudes. Francis and Vavrus (2012) suggest Arctic sea ice loss could lead to weaker zonal jets plus planetary waves with meridionally amplified undulations. The subject is controversial as the trend studies of Barnes (2013) and Screen and Simmonds (2013) did not find clear statistical evidence in support of wave amplification.

Studies of extratropical sea surface temperature (SST) anomalies provide some insight into how sea ice changes affect nonlocal climate. The response to the

anomalies typically shows a fast, local, more or less predictable baroclinic response (lower-tropospheric warming and decreasing surface pressure near positive SST anomalies) followed by a barotropic response of larger magnitude and much greater horizontal extent (e.g., Kushnir et al. 2002; Li and Conil 2003; Ferreira and Frankignoul 2005). The nonlocal impacts are frequently small compared to internal variability and are, thus, difficult to reliably detect (Kushnir et al. 2002; Magnusdottir et al. 2004; Screen et al. 2013, 2014). These complicated impacts involve nonlinear processes through eddy fluxes and are highly dependent on time of year, linkage to storm tracks, and the large-scale flow (Peng and Whitaker 1999; Magnusdottir et al. 2004; Screen et al. 2012; Seo et al. 2014; Vihma 2014). The baroclinic stage is perhaps 10 days, while it may take months for equilibrium to be reached in the barotropic response (Li and Conil 2003; Deser et al. 2007; Jung et al. 2014; Seo et al. 2014). The response can modulate primary climate modes of variability (Ferreira and Frankignoul 2005; Seo et al. 2014). In particular, modeling studies have linked negative Arctic sea ice anomalies to the negative phase of the North Atlantic Oscillation (e.g., Magnusdottir et al. 2004; Seierstad and Bader 2009; Screen et al. 2013; Tang et al. 2013). Several studies show the surprising finding that warming in the Arctic associated with sea ice changes can correlate to localized regions of cooling in the midlatitudes (e.g., Alexander et al. 2004; Tang et al. 2013; Vihma 2014). Royer et al. (1990) modeled surface cooling of up to 3 K over northern Eurasia. There is recent support as Yang

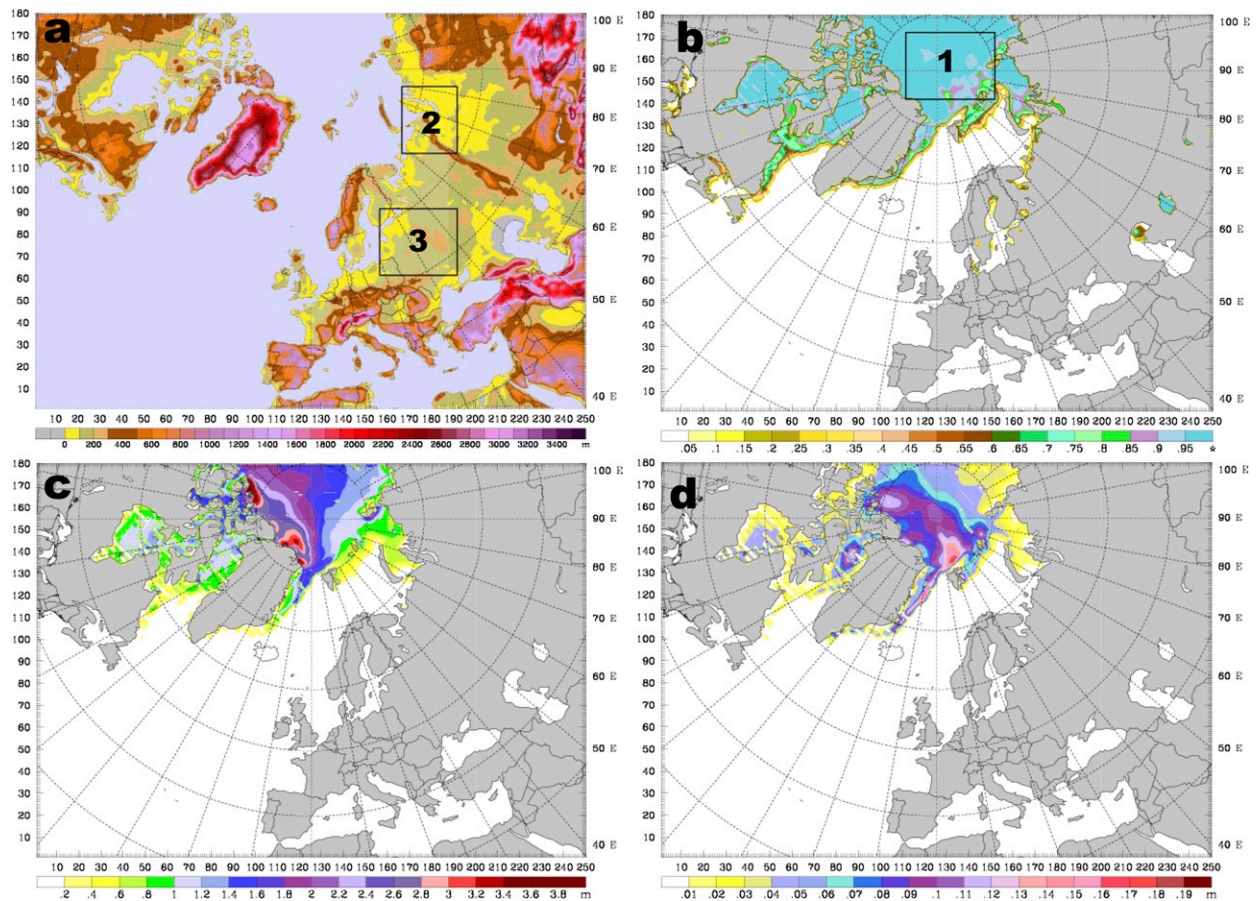


FIG. 8. Map of domain showing 0000 UTC 24 Jan 2012 values of (a) topography (m), (b) sea ice concentration (fraction), (c) sea ice thickness (m), and (d) snow depth on sea ice (m). The numbered boxes are for time series.

and Christensen (2012) find an ensemble of 13 Coupled Model Intercomparison Project Phase 5 (CMIP5) models shows that cold European Januaries are linked to warm Arctic anomalies and the negative phase of the Arctic Oscillation, which is usually in phase with the North Atlantic Oscillation. Some caution must be applied in interpreting cause and effect in observed cases, since sea ice anomalies may result from atmospheric anomalies (e.g., Simmonds and Govekar 2014). Preliminary Polar WRF simulations for a synoptic case study with thinning Arctic sea ice on the new grid showed cooling over Europe.

We simulate a 24 January–7 February 2012 case study, a period characterized by blocking. Blocking could lead to anomalous northerly flow from the Arctic, which has been shown to increase the teleconnection between the Arctic and midlatitudes (Jung et al. 2014). During this time the sea ice thickness distribution displayed in Fig. 8c includes relatively thin ice north of Russia, frequently less than 1.5 m thick. Thicker ice is present north of Canada and Greenland with local

maxima in excess of 3 m. Initial and boundary conditions for the simulations of this time period are from the National Centers for Environmental Prediction's Global Forecast System (GFS) Final Operational Global Analysis (FNL). The simulations for this case study are continuous with no spectral nudging, because the goal is to show the full unhindered response. Ensembles are used to gauge the statistical significance to sea ice thickness changes. Because of the specified horizontal boundaries, the response to the specified anomalies is limited. Since many studies with global models have investigated the sensitivity to Arctic sea ice change, we deem it unnecessary to repeat that comprehensive test. We run four different cases with Polar WRF (Table 5). Five ensemble members are run for each case formed by randomly varying the specified isothermal stratospheric temperature that is used for the hydrostatically balanced reference state partition of the anelastic calculations. Instead of the standard temperature 200 K, the isothermal reference state is varied between 198 and 202 K for the stratosphere. The four sensitivity tests each have

TABLE 5. Numerical simulations with Polar WRF 3.5 for 24 Jan–7 Feb 2012.

Simulation	Sea ice thickness (m)	Snow depth (m)	Ensemble
Remote0.1m	0.1	Variable	5
Remote0.5m	0.5	Variable	5
Remote1m	1	Variable	5
Remote3m	3	Variable	5

the same spatially variable snow depths taken from the PIOMAS analysis, with the specified ice thicknesses uniform in space and time for each case at 3, 1, 0.5, or 0.1 m (Table 5).

7. Results of case study 2

Figure 9 shows selected snapshots of the observed 500-hPa fields from the GFS FNL simulation. During late January and early February 2012, the circumpolar vortex at 500 hPa is offset from the North Pole toward northern Canada. Several highs and lows break the eastward flow over Europe, resulting in strong blocking. The time 0000 UTC 1 February is a representative example with a ridge present along the Arctic Ocean coast and a low to the south over eastern Europe (Fig. 9e).

During the case study a strong, persistent surface high (not shown) develops over northern Eurasia and extends from Scandinavia eastward to the Siberian Arctic. The associated sea level pressure maximum exceeds

1060 hPa on 1 February. North of the surface high, westerly winds carry relatively warm air over the Arctic Ocean. To the south, in contrast, cooling occurs over central and eastern Europe in late January, eventually reaching western Europe by 1 February. Lowest temperatures for western Europe occur near 3 February. During February, a surface low develops over the southern Arctic Ocean as part of a frontal system and a very strong warm front moves over Russia.

Figure 10 shows selected snapshots of the sea level pressure difference between ensemble averages for the 0.5-m case (Remote0.5m) and 3-m cases (Remote3m). The patterns show characteristic differences between ensembles for thinner and thicker sea ice. The different sea ice specifications directly impact the ice-covered area of the Arctic Ocean, including box 1 in Fig. 8b. The sea level pressure northeast of Greenland quickly responds to the forcing. Figures 10a and 10b for the 48- and 84-h difference fields, respectively, indicate a pressure reduction by 1–1.5 hPa over the central Arctic in Remote0.5m. Pressure is also reduced west of Greenland in the thinner sea ice ensemble. The pressure differences between simulations are small, however, over much of the domain during the first few days of the simulation (Figs. 10a,b). The early response is analogous to the fast, local baroclinic response to extratropical SST anomalies.

Figure 11 displays time series for box 1 in the central Arctic shown in Fig. 8b. The use of ensembles enables determination of the statistical significance for the sensitivity tests. The significance of ensemble differences is

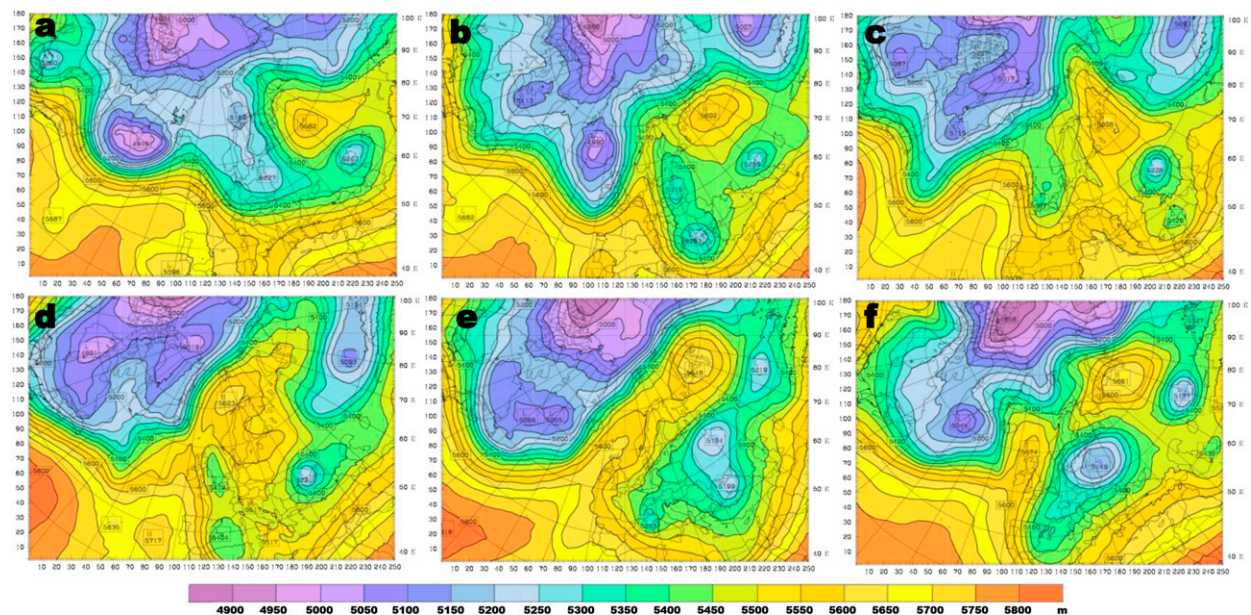


FIG. 9. Geopotential height (geopotential meters, gpm) at 500 hPa from NCEP GFS FNL for (a) 0000 UTC 24 Jan, (b) 0000 UTC 26 Jan, (c) 0000 UTC 28 Jan, (d) 0000 UTC 30 Jan, (e) 0000 UTC 1 Feb, and (f) 0000 UTC 3 Feb 2012. Contour interval is 50 gpm.

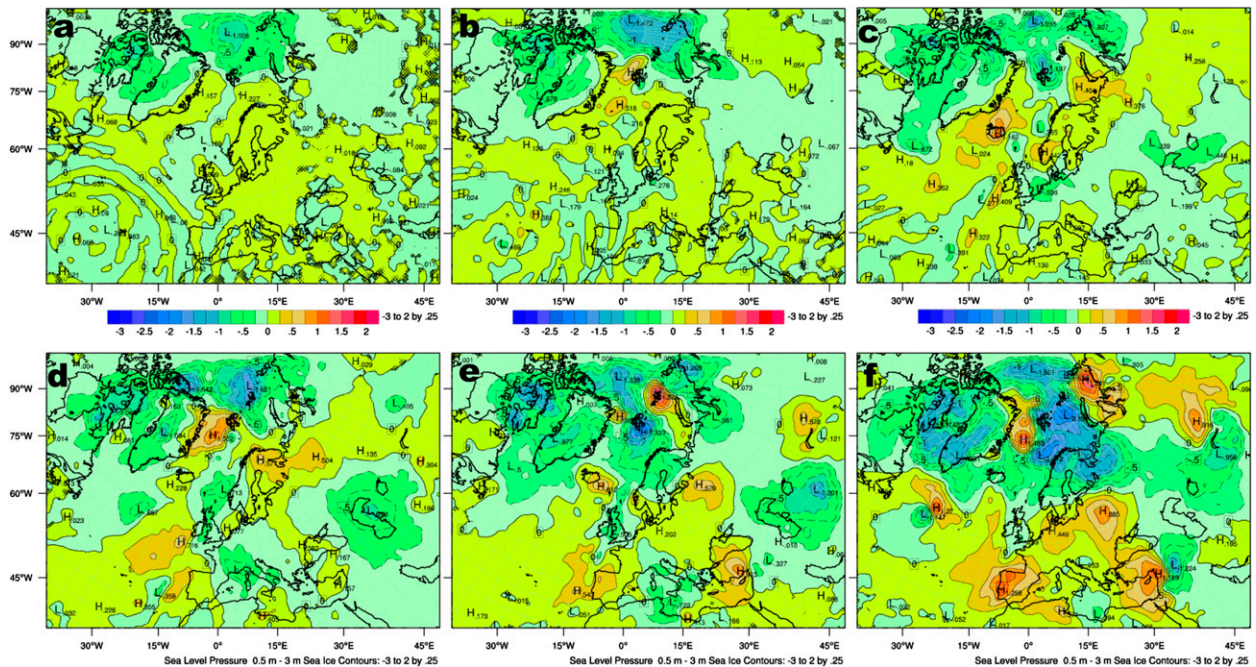


FIG. 10. Mean sea level pressure difference (hPa) between the Remote0.5m and Remote3m simulations for (a) 0000 UTC 26 Jan (hour 48), (b) 1200 UTC 27 Jan (hour 84), (c) 0000 UTC 29 Jan (hour 120), (d) 1200 UTC 30 Jan (hour 156), (e) 0000 UTC 31 Jan (hour 168), and (f) 0000 UTC 1 Feb 2012 (hour 192). Contour interval is 0.25 hPa.

calculated with the Student's t test starting on 1 February (Julian day 32). A robust significance test is sought for sensitivity to sea ice thickness. Therefore, we especially seek times when ensemble average quantities have differences (Remote3m – Remote0.5m and Remote1m – Remote0.1m) of the same sign and are *both statistically significant*. For each time series in Figs. 11 and 12 (see also Fig. 14), times when both differences are statistically significant at the 95% confidence level are shown between single right-pointing and left-pointing arrows. When both differences meet the 99% confidence threshold, double arrows are shown. However, frequently the difference between individual ensemble members is similar in magnitude to the differences between ensemble averages; thus, the criteria for robust statistical significance are not satisfied. Ensemble-average differences are typically largest between Remote0.1m and Remote3m quantities, and statistical thresholds are most readily met by this comparison. Therefore, to display weaker examples of significant sensitivity to sea ice thickness, pairs of asterisks bound times when the 90% confidence limit is achieved for the ensemble difference Remote3m – Remote0.1m, and the more stringent criteria are not met.

Figure 11a shows that setting smaller values for the sea ice thickness warms the surface temperature several degrees within a few hours. By February, the difference

between the 0.1- and 3-m ice thickness ensembles is 8–10K. The simulations Remote0.5m and Remote1m show intermediate responses inversely related to ice thickness. The sections of the time series between double arrows show that the surface impact of sea ice thickness is highly statistically significant.

The average sea level pressure in box 1 is displayed in Fig. 11b. The hydrostatic impact associated with the thermal forcing typically results in lower sea level pressures over thinner sea ice (Fig. 11b). The response of the sea level pressure field to the forcing is more complicated, however, than that of surface temperature. The pressure response is relatively small during January. During the first week of the test period the response is most obvious in Remote0.1m, the warmest ensemble for the sea ice region. The pressure responses in Fig. 11b become larger beginning about Julian day 32 (1 February). Unfortunately, the signal-to-noise ratio is too small for the sea level pressure difference to be regarded as significantly different than zero according to more stringent criteria. Only the region between the asterisks for 0600–1200 UTC 7 February meets the 90% confidence limit for the Remote3m – Remote0.1m pressure difference. In contrast to the sea level pressure results, central Arctic 500-hPa heights are typically highest in Remote0.1m and lowest in Remote3m (Fig. 11c). The thickness between the 1000- and 500-hPa isobaric levels

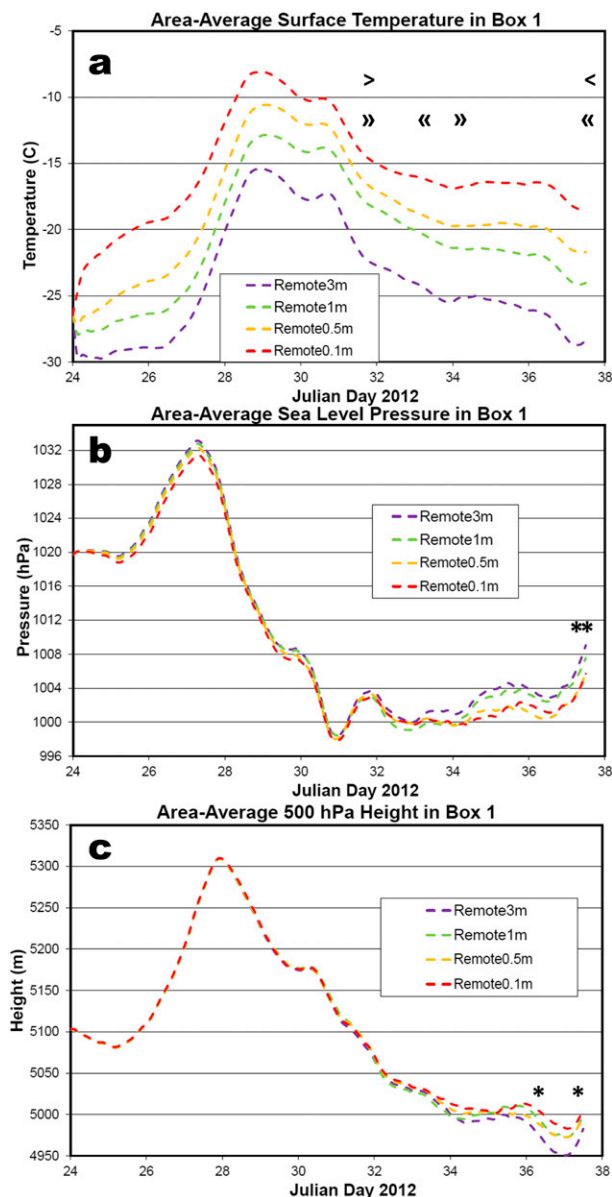


FIG. 11. Time series for box 1 in Fig. 8b showing area-average (a) surface temperature ($^{\circ}\text{C}$), (b) mean sea level pressure (hPa), and (c) 500-hPa height (gpm). Times between the asterisks, arrows, or double arrows are within statistical confidence levels (see text).

(not shown) varies by about 30 m between ensembles during the last few days of the simulations, and of is similar weak statistical significance. Furthermore, there is evidence toward a slight weakening in the circumpolar vortex in the troposphere in the experiments with thinner sea ice settings. Accordingly, average wind speed (not shown) in the middle troposphere is slightly reduced north of 60°N in the thinner sea ice cases. A weakening of the elevated westerly circulation in high

latitudes in response to reduced Arctic sea ice is consistent with the findings of Francis and Vavrus (2012).

To explore the transmission from the sea ice vertically into the atmosphere for the ensembles, Fig. 12 shows heat conduction flux and sensible heat flux for box 1. As was seen in section 5, thinner sea ice allows larger heat flux through ice from the ocean to the interface with the atmosphere (Fig. 6). Accordingly, the average heat conduction flux for 0000 UTC 24 January–0000 UTC 7 February is 49.7 W m^{-2} for the Remote0.1m ensemble, but only 12.6 W m^{-2} for Remote3m. Heat is then transferred from the earth’s surface into the atmosphere through the sensible heat flux. Average sensible heat flux for Remote3m during this time is -1.1 W m^{-2} . Therefore, the turbulent flux is actually cooling the atmosphere for that thick ice ensemble. The average is positive, however, and warming the atmosphere in the other experiments, with the largest average sensible heat flux, 10.2 W m^{-2} , in Remote0.1m. Latent heat flux (not shown) is also warming the atmosphere, but its magnitude is about half that of the sensible heat flux. In summary, heat is transferred by conduction within the sea ice up from the ocean to the interface with the atmosphere, and this is enhanced in cases with thinner sea ice. More than a week is required, however, before marginally statistically significant impacts are seen in the sea level pressure and 500-hPa height for box 1 in the Arctic sea ice region (Figs. 11b,c).

To demonstrate nonlocal impacts, Fig. 13 shows snapshots of the sea level pressure and 2-m temperature fields at 0000 UTC 3 February for Remote0.5m and Remote3m. A strong frontal cyclone is seen over northern Europe with a distinct warm sector, warm front, and cold front. Since the cyclone is adjacent to box 1, it can be influenced by the sea ice specifications over the Arctic Ocean. Accordingly, box 1 is colder over the thicker sea ice in the Remote3m experiment than in Remote0.5m. The modulated cyclone shows slightly different sea level pressure gradients between panels in Fig. 13. The horizontal pressure gradient in Fig. 13b has a greater component perpendicular to the western boundary of box 2 in this thicker sea ice case. Thus, the warm front propagates eastward slightly faster in Remote3m.

The 850-hPa temperature field is modulated by the frontal progression rates. Figure 14 shows times series for this field for the three boxes shown in Fig. 8. Even over the sea ice, the temperature differences between ensembles are very small at 850 hPa during January (Fig. 14a). Evidently, a spinup of at least a week is required for the surface forcing to become very noticeable in the free atmosphere. A small impact on 850-hPa temperature is visible a little earlier for

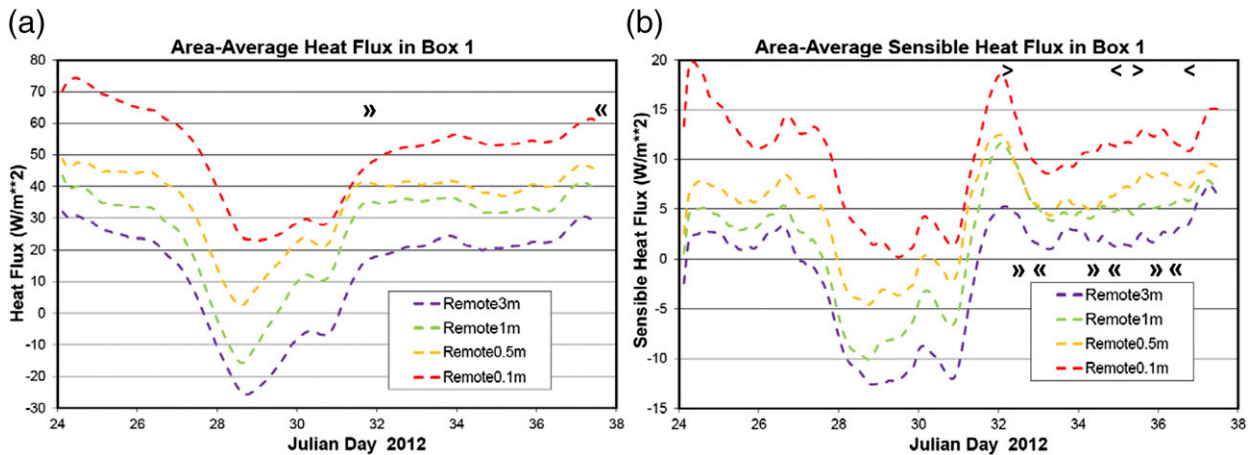


FIG. 12. Time series for the Arctic box 1 in Fig. 8b showing area-average (a) heat flux up to the surface ($W m^{-2}$), and (b) sensible heat flux ($W m^{-2}$) for the 24 Jan–7 Feb 2012 Polar WRF ensemble averages. Times between arrows or double arrows are within statistical confidence levels (see text).

Remote0.1m than in the other ensembles. Since that is locally the warmest case, the associated weaker static stability in the boundary layer may allow a somewhat faster response into the free atmosphere. It is interesting that the timing of the 850-hPa temperature divergence between experiments is surprisingly similar for all three boxes.

Boxes 2 and 3 in Fig. 8a are used to detail responses to ice thickness specification in locations outside the Arctic sea ice region. Box 2 near the Ural Mountains of Eurasia shows little difference in 850-hPa temperature between ensembles until 1 February (Julian day 32) and, then, a

sharp increase through 3 February (Fig. 14b) influenced by the warm frontal passage. The criteria for confidence at the 95% level are reached for 1200 UTC 2 February–0000 UTC 3 February. Interestingly, the response is opposite in Fig. 14b to that in Fig. 14a in that the thicker Arctic sea ice ensembles are actually associated with warmer temperature in box 2.

Box 3 over western Russia displays an alternative sensitivity to sea ice thickness to that in box 2 (Fig. 14c). The 850-hPa temperature in box 3 increases fastest during early February in the thinnest sea ice ensemble. Figures 14a and 14c show only marginal statistical

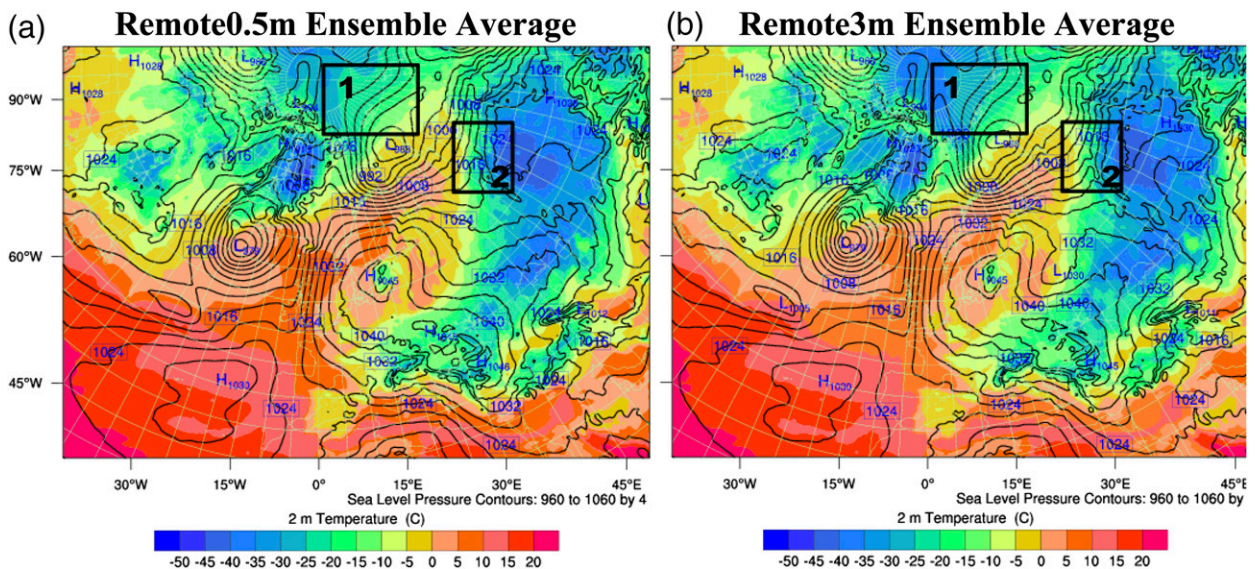


FIG. 13. Mean sea level pressure (contours, hPa) and 2-m temperature (color scale, $^{\circ}C$) from ensemble averages for the (a) Remote0.5m and (b) Remote3m cases at 0000 UTC 3 Feb 2012. Pressure contour is 4 hPa. Boxes 1 and 2 are for time series.

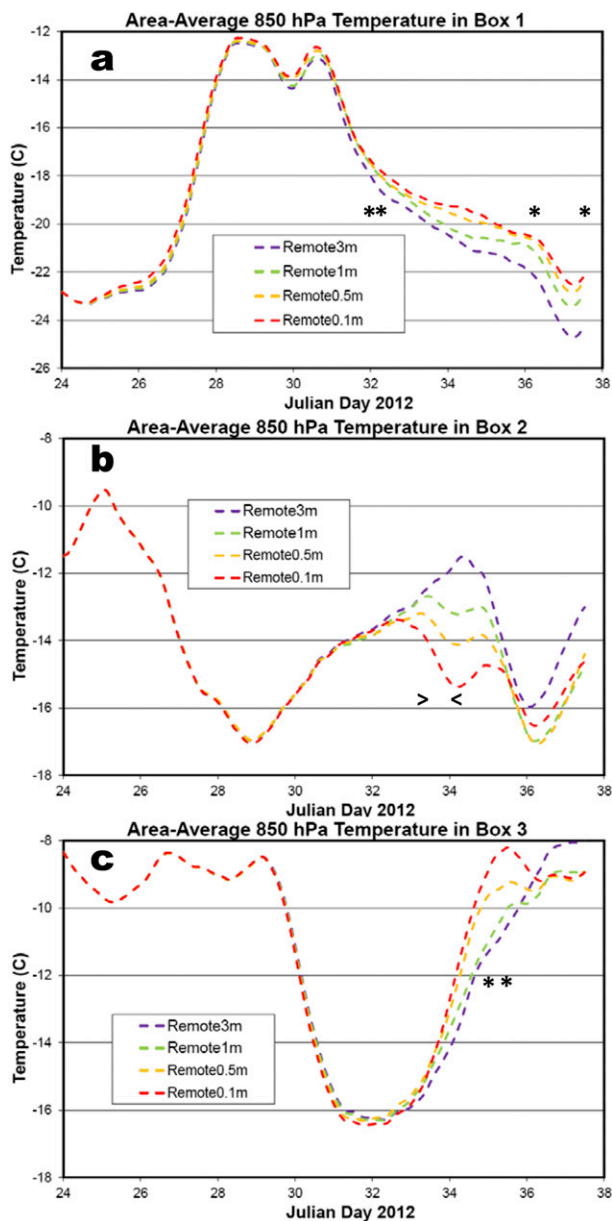


FIG. 14. Time series for the boxes in Fig. 8 show area-average 850-hPa temperatures for boxes (a) 1, (b) 2, and (c) 3. Times between the asterisks or arrows are within statistical confidence levels (see text).

significance, as the differences between ensembles on 3 February are half or less than that shown in Fig. 14b. While the response in 850-hPa temperature in box 2 is a transient response during a simulation of two weeks, it is interesting to note that the largest difference between ensembles was not found over the Arctic sea ice. Thus, the 850-hPa temperature time series show evidence for a complicated response at sub-Arctic locations to changes in the Arctic sea ice thickness. On synoptic time scales, a thinning of Arctic sea ice, while locally inducing a

warming response in the high Arctic, can induce cooling responses at some midlatitude locations, as shown in some previous climate simulations. Much longer simulations beyond the scope of this paper are required for a more thorough evaluation of the climatological response pattern. Nevertheless, the simulations presented here suggest that the thinning sea ice over recent decades can enhance the much more widely explored response to reductions in Arctic sea ice area.

8. Summary and conclusions

Polar WRF simulations show local and nonlocal impacts from the specification of sea ice thickness and snow depth over sea ice. Polar WRF, a polar-optimized code supplement to the standard WRF configuration, is available to the scientific community for Arctic and Antarctic applications. Versions of Polar WRF up to 3.4 include sea ice modifications to the Noah land surface model that allow users to specify ice thickness rather than using a default thickness of 3 m, and specify snow depth on sea ice rather than having it partially constrained toward 0.05 m. Specified variable sea ice thickness and snow depth over sea ice are now options in the standard WRF release starting with WRF V3.5. Previously, it was difficult to obtain gridded, time- and space-varying analyzed values of ice thickness and snow over sea ice. Fortunately, new Arctic datasets for these fields have become available recently. Furthermore, some observational guidance on sea ice thickness and snow depth also exists for the Southern Hemisphere (e.g., Steinhoff et al. 2013). Consequently, we test the impact of specified sea ice thickness and snow depth over sea ice with Arctic Polar WRF 3.5 simulations, including some ensemble cases.

For the local response in the lower troposphere we select the very well-observed 1997/98 SHEBA case as a test period. In particular, January 1998 is chosen as the air-sea temperature difference is large. The Arctic grid for this case has 20-km grid spacing and 39 vertical levels. A control simulation with the default Noah settings (i.e., 3-m sea ice thickness and 0.05-m snow depth on sea ice) in WRF is compared with a Polar WRF simulation with specified variable sea ice thickness and snow depth over sea ice taken from the recent PIOMAS analysis. Several sensitivity tests with five-member ensembles evaluate the different specified sea ice thicknesses and snow depths. Both ice thickness and snow have a noticeable impact on simulated near-surface temperature, primarily by impacting the heat transfer through snow and ice. Differences between ensemble averages for the sensitivity tests are up to 5°C, which is larger than the temperature bias in the standard WRF

3.5 and Polar WRF 3.5 simulations, and similar in magnitude to the root-mean-square errors of the forecasts. Therefore, it is important to obtain good representations of the ice thickness and snow depth in polar simulations. Compared to the average of all Arctic sea ice grid points, ice station SHEBA is several degrees colder. The sensitivity to sea ice thickness and snow at SHEBA, however, appears to be qualitatively similar to the average for Arctic sea ice. Thus, SHEBA appears to be a realistic test bed for the sensitivity simulations.

Nonlocal impacts of specified sea ice thickness and snow cover are examined with a synoptic case study. The 24 January–7 February 2012 blocking event is simulated with a 40-km grid but retaining 39 vertical levels. The grid includes Europe and parts of the North Atlantic and Arctic Oceans. Ensemble simulations indicate that thinner sea ice reduces central Arctic sea level pressure and increases midtropospheric geopotential heights during the winter case study period. It takes about one week for noticeable impacts to be seen in the mid-latitudes. The remote responses to the changed representations of sea ice thickness, however, are variable and complex. As the test period here has been limited to two weeks, future work is required to determine how the far-field responses may evolve over longer periods of simulation.

Acknowledgments. This research is supported by NSF Grants ARC-0733023, ARC-1144117, ANT-1049089, and ANT-1135171, and NASA Grants NNX12AI29G and NNX14CK47C. Numerical simulations were performed on the Intel Xeon cluster at the Ohio Supercomputer Center, which is supported by the state of Ohio, and on NCAR’s Computational and Information Systems Laboratory’s Yellowstone, supported by NSF. We thank Jinlun Zhang and Ron Lindsay of the University of Washington for supplying PIOMAS sea ice thickness and snow depth on sea ice. We thank Jonas Martin of Stockholm University and Mark Anderson of the University of Nebraska for supplying sea ice freeze and thaw dates.

APPENDIX

Implementation of Variable Sea Ice Thickness and Snow Depth in the WRF Noah LSM

Sea ice fraction was first implemented into Polar WRF by Bromwich et al. (2009). The contributions of the ice fraction, ICE, and ocean fraction, $(1 - \text{ICE})$, of a grid cell toward a net quantity A are summed through the mosaic method, $A = \text{ICE}A_i + (1 - \text{ICE})A_w$, where the subscripts i and w refer to the ice and open water

fractions, respectively. The surface values of temperature, specific humidity, and the surface fluxes are partitioned this way. At a sea ice grid point, prior to applying the near-surface component to the atmospheric boundary layer scheme and the LSM, the temperature and specific humidity at the surface for the ice fraction are extracted by a “wrapper” routine. After the LSM and surface boundary layer computations, the net values for the entire grid point are reassembled. The values for the water fraction are provided by an independent call to the surface boundary layer scheme.

To add sea ice thickness and snow depth on sea ice into the Noah LSM for Polar WRF, variables SITHIK and SNOWSI are added to the WRF registry of variables. The addition allows these fields to be input through the standard initialization method using the WRF preprocessing system (Wang et al. 2013). For versions 3.5 and 3.6, ICEDEPTH replaces SITHIK. The sea ice physics for WRF Noah was placed outside the main land module starting with version 3.4. The basic representation of ice thickness and snow depth, however, remains similar for sea ice grid points. Thickness is restricted within 0.1–10 m, while snow depth is restricted within 0.001–1 m. Previously, thickness was set at 3 m, while snow depth was initialized at 0.05 m.

Sea ice thickness and snow depth impact the thermodynamics through heat transfer calculations and the determination of skin temperature. The Noah LSM uses four subsurface layers with a snow layer on top. Prognostic temperatures are computed for the four layers. For standard soil, layer depth varies from 0.1 m for the top layer to 1 m for the bottom layer. Over sea ice, however, all four layers are set with identical thicknesses:

$$\text{ZSOIL} = \text{SITHIK}/\text{NSOIL}, \quad (\text{A1})$$

where ZSOIL is the total thickness of each layer and NSOIL is the number of layers. For snow depth on sea ice, the snow height, ZSNOW, is simply set as SNOWSI. In WRF Noah, the distance between the top of the snow layer (when snow is present) and the midpoint of the upper subsurface layer is used to calculate the heat flux up through the snow layer:

$$G = -\text{DF1}(T_S - T_1)/(0.5\text{ZSOIL}_1 + \text{ZSNOW}) \quad \text{and} \quad (\text{A2})$$

$$\begin{aligned} \text{DF1} = & (D_{\text{SNOW}}\text{ZSNOW} \\ & + 0.5D_{\text{ICE}}\text{ZSOIL}_1)/(0.5\text{ZSOIL}_1 + \text{ZSNOW}), \end{aligned} \quad (\text{A3})$$

Where DF1 is the net thermal conductivity of a combination of snow, D_{SNOW} , and ice, D_{ICE} ($2.2 \text{ W m}^{-1} \text{ K}^{-1}$).

The variables T_S and T_1 are the effective snow surface and midpoint of the top subsurface layer temperatures, respectively, and $ZSOIL_1$ is the total thickness of the top subsurface layer. Clearly, a deeper snow layer over sea ice will reduce the heat flux in Eq. (A2). Previously, the thermal conductivity of snow (in $W m^{-1} K^{-1}$) was obtained as a function of density from the formula

$$D_{SNOW} = 0.0763 \times 10^{(2.25 \text{Density})}, \quad (\text{A4})$$

where Density is the density of snow (in $g cm^{-3}$). A snow depth of 0.05 m of snow at a density of $0.3 g cm^{-3}$ would have a conductivity of $0.361 W m^{-1} K^{-1}$, while net conductivity DF1 would be $1.28 W m^{-1} K^{-1}$. Starting with version 3.4.1, Polar WRF's thermal conductivity for snow over sea ice is set at $0.3 W m^{-1} K^{-1}$ (Sturm et al. 2002; Persson 2012).

WRF Noah computes an effective snow surface temperature diagnostically by setting the left-hand side of Eq. (1) to zero and adjusting only H_s and G as a function of T_S . Relevant additional modifications for Polar WRF include modifying the lookup tables to increase the ice emissivity to 0.98, increasing the moisture availability to 1, setting the surface roughness at 0.001 m, and increasing the summer glacier albedo to 0.7 and the winter glacier albedo to 0.8.

REFERENCES

- Alexander, M. A., U. S. Bhatt, J. E. Walsh, M. S. Timlin, J. S. Miller, and J. D. Scott, 2004: The atmospheric response to realistic Arctic sea ice anomalies in an AGCM during winter. *J. Climate*, **17**, 890–905, doi:10.1175/1520-0442(2004)017<0890:TARTRA>2.0.CO;2.
- Barnes, E. A., 2013: Revisiting the evidence linking Arctic amplification to extreme weather in midlatitudes. *Geophys. Res. Lett.*, **40**, 4734–4739, doi:10.1002/grl.50880.
- Berg, P., R. Döscher, and T. Koenigk, 2013: Impacts of using spectral nudging on regional climate model RCA4 simulations of the Arctic. *Geosci. Model Dev. Discuss.*, **6**, 495–520, doi:10.5194/gmdd-6-495-2013.
- Bromwich, D. H., K. M. Hines, and L.-S. Bai, 2009: Developments and testing of Polar Weather Research and Forecasting model: 2. Arctic Ocean. *J. Geophys. Res.*, **114**, D08122, doi:10.1029/2008JD010300.
- , Y.-H. Kuo, M. C. Serreze, J. E. Walsh, L. S. Bai, M. Barlage, K. M. Hines, and A. S. Slater, 2010: Arctic System Reanalysis: Call for community involvement. *Eos, Trans. Amer. Geophys. Union*, **91**, 13–14, doi:10.1029/2010EO020001.
- , F. O. Otieno, K. M. Hines, K. W. Manning, and E. Shilo, 2013: Comprehensive evaluation of polar weather research and forecasting performance in the Antarctic. *J. Geophys. Res. Atmos.*, **118**, 274–292, doi:10.1029/2012JD018139.
- Cassano, E. N., J. J. Cassano, M. E. Higgins, and M. C. Serreze, 2014: Atmospheric impacts of an Arctic sea ice minimum as seen in the Community Atmosphere Model. *Int. J. Climatol.*, **34**, 766–779, doi:10.1002/joc.3723.
- Cassano, J. J., M. E. Higgins, and M. W. Seefeldt, 2011: Performance of the Weather Research and Forecasting (WRF) Model for month-long pan-Arctic simulations. *Mon. Wea. Rev.*, **139**, 3469–3488, doi:10.1175/MWR-D-10-05065.1.
- Chen, F., and J. Dudhia, 2001: Coupling an advanced land surface–hydrology model with the Penn State–NCAR MM5 modeling system. Part I: Model implementation and sensitivity. *Mon. Wea. Rev.*, **129**, 569–585, doi:10.1175/1520-0493(2001)129<0569:CAALSH>2.0.CO;2.
- Clough, S. A., M. W. Shephard, E. J. Mlawer, J. S. Delamere, M. J. Iacono, K. Cady-Pereira, S. Boukabara, and P. D. Brown, 2005: Atmospheric radiative transfer modeling: A summary of the AER codes. *J. Quant. Spectrosc. Radiat. Transfer*, **91**, 233–244, doi:10.1016/j.jqsrt.2004.05.058.
- Comiso, J. C., 2000: Bootstrap sea ice concentrations from Nimbus-7 SMMR and DMSP SSM/I-SSMIS: Version 2. NASA/DAAC at the National Snow and Ice Data Center, accessed 17 October 2007, doi:10.5067/J6JQLS9EJ5HU.
- , C. L. Parkinson, R. Gersten, and L. Stock, 2008: Accelerated decline in Arctic sea ice cover. *Geophys. Res. Lett.*, **35**, L01703, doi:10.1029/2007GL031972.
- Dee, D. P., and Coauthors, 2011: The ERA-Interim reanalysis: Configuration and performance of the data assimilation system. *Quart. J. Roy. Meteor. Soc.*, **137**, 553–597, doi:10.1002/qj.828.
- Deser, C., R. A. Tomas, and S. Peng, 2007: The transient atmospheric circulation response to North Atlantic SST and sea ice anomalies. *J. Climate*, **20**, 4751–4767, doi:10.1175/JCLI4278.1.
- , R. Tomas, M. Alexander, and D. Lawrence, 2010: The seasonal atmospheric response to projected Arctic sea ice loss in the late twenty-first century. *J. Climate*, **23**, 333–351, doi:10.1175/2009JCLI3053.1.
- Ferreira, D., and C. Frankignoul, 2005: The transient atmospheric response to midlatitude SST anomalies. *J. Climate*, **18**, 1049–1067, doi:10.1175/JCLI-3313.1.
- Francis, J. A., and S. J. Vavrus, 2012: Evidence linking Arctic amplification to extreme weather in mid-latitudes. *Geophys. Res. Lett.*, **39**, L06801, doi:10.1029/2012GL051000.
- , W. Chan, D. J. Leathers, J. R. Miller, and D. E. Veron, 2009: Winter Northern Hemisphere weather patterns remember summer Arctic sea-ice extent. *Geophys. Res. Lett.*, **36**, L07503, doi:10.1029/2009GL037274.
- Glisan, J. M., W. J. Gutowski, J. J. Cassano, and M. E. Higgins, 2013: Effects of spectral nudging in WRF on Arctic temperature and precipitation simulations. *J. Climate*, **26**, 3985–3999, doi:10.1175/JCLI-D-12-00318.1.
- Grell, G. A., and S. R. Freitas, 2013: A scale and aerosol aware stochastic convective parameterization for weather and air quality modeling. *Atmos. Chem. Phys.*, **13**, 23 845–23 893, doi:10.5194/acpd-13-23845-2013.
- Hines, K. M., and D. H. Bromwich, 2008: Development and testing of Polar WRF. Part I: Greenland Ice Sheet meteorology. *Mon. Wea. Rev.*, **136**, 1971–1989, doi:10.1175/2007MWR2112.1.
- , —, L. S. Bai, M. Barlage, and A. G. Slater, 2011: Development and testing of Polar WRF. Part III: Arctic land. *J. Climate*, **24**, 26–48, doi:10.1175/2010JCLI3460.1.
- Honda, M., J. Inoue, and S. Yamane, 2009: Influence of low Arctic sea-ice minima on anomalously cold Eurasian winters. *Geophys. Res. Lett.*, **36**, L08707, doi:10.1029/2008GL037079.
- Hudson, S. R., M. A. Granskog, A. Sundfjord, A. Randelhoff, A. H. H. Renner, and D. V. Divine, 2013: Energy budget of first-year Arctic sea ice in advanced stages of melt. *Geophys. Res. Lett.*, **40**, 2679–2683, doi:10.1002/grl.50517.

- Jaiser, R., K. Dethloff, D. Handorf, A. Rinke, and J. Cohen, 2012: Impact of sea ice cover changes on the Northern Hemisphere atmospheric winter circulation. *Tellus*, **64A**, 11595, doi:10.3402/tellusa.v64i0.11595.
- Jung, T., M. A. Kasper, T. Semmler, and S. Serrar, 2014: Arctic influence on subseasonal midlatitude prediction. *Geophys. Res. Lett.*, **41**, 3676–3680, doi:10.1002/2014GL059961.
- Kay, J. E., M. M. Holland, and A. Jahn, 2011: Inter-annual to multi-decadal Arctic sea ice extent trends in a warming world. *Geophys. Res. Lett.*, **38**, L15708, doi:10.1029/2011GL048008.
- Kern, S., and G. Spreen, 2015: Uncertainties in Antarctic sea-ice thickness retrieval from ICESat. *Ann. Glaciol.*, **56**, 107–119, doi:10.3189/2015AoG69A736.
- Kushnir, Y., W. A. Robinson, I. Bladé, N. M. J. Hall, S. Peng, and R. Sutton, 2002: Atmospheric GCM response to extratropical SST anomalies: Synthesis and evaluation. *J. Climate*, **15**, 2233–2256, doi:10.1175/1520-0442(2002)015<2233:AGRTE>2.0.CO;2.
- Kwok, R., and D. A. Rothrock, 2009: Decline in Arctic sea ice thickness from submarine and ICESat records: 1958–2008. *Geophys. Res. Lett.*, **36**, L15501, doi:10.1029/2009GL039035.
- , and N. Untersteiner, 2011: Decline in Arctic sea ice thickness from submarine and ICESat records: 1958–2008. *Phys. Today*, **64**, 36–43, doi:10.1063/1.3580491.
- , G. F. Cunningham, M. Wensnahan, I. Rigor, H. J. Zwally, and D. Yi, 2009: Thinning and volume loss of the Arctic Ocean sea ice cover: 2003–2008. *J. Geophys. Res.*, **114**, C07005, doi:10.1029/2009JC005312.
- Laxon, S. W., and Coauthors, 2013: CryoSat-2 estimates of Arctic sea ice thickness and volume. *Geophys. Res. Lett.*, **40**, 732–737, doi:10.1002/grl.50193.
- Ledley, T. S., 1988: For a lead-temperature feedback in climatic variation. *Geophys. Res. Lett.*, **15**, 36–39, doi:10.1029/GL015i001p00036.
- , 1993: Variations in snow on sea ice: A mechanism for producing climate variations. *J. Geophys. Res.*, **98**, 10401–10410, doi:10.1029/93JD00316.
- Li, Z. X., and S. Conil, 2003: Transient response of an atmospheric GCM to North Atlantic SST anomalies. *J. Climate*, **16**, 3993–3998, doi:10.1175/1520-0442(2003)016<3993:TROAAG>2.0.CO;2.
- Lindsay, R. W., J. Zhang, A. Schweiger, M. Steele, and H. Stern, 2009: Arctic sea ice retreat in 2007 follows thinning trend. *J. Climate*, **22**, 165–176, doi:10.1175/2008JCLI2521.1.
- Magnusdottir, G., C. Deser, and R. Saravanan, 2004: The effects of North Atlantic SST and sea ice anomalies on the winter circulation in CCM3. Part I: Main features and storm track characteristics of the response. *J. Climate*, **17**, 857–876, doi:10.1175/1520-0442(2004)017<0857:TEONAS>2.0.CO;2.
- Maslanik, J. A., C. Fowler, J. Stroeve, S. Drobot, J. Zwally, D. Yi, and W. Emery, 2007: A younger, thinner Arctic ice cover: Increased potential for rapid, extensive sea-ice loss. *Geophys. Res. Lett.*, **34**, L24501, doi:10.1029/2007GL032043.
- , J. Stroeve, C. Fowler, and W. Emery, 2011: Distribution and trends in Arctic sea ice age through spring 2011. *Geophys. Res. Lett.*, **38**, L13502, doi:10.1029/2011GL047735.
- Morrison, H., J. A. Curry, and V. I. Khvorostyanov, 2005: A new double-moment microphysics parameterization for application in cloud and climate models. Part I: Description. *J. Atmos. Sci.*, **62**, 1665–1677, doi:10.1175/JAS3446.1.
- Murray, R. J., and I. Simmonds, 1995: Responses of climate and cyclones to reductions in Arctic winter sea ice. *J. Geophys. Res.*, **100**, 4791–4806, doi:10.1029/94JC02206.
- Nakanishi, M., and H. Niino, 2006: An improved Mellor–Yamada level-3 model: Its numerical stability and application to a regional prediction of advection fog. *Bound.-Layer Meteor.*, **119**, 397–407, doi:10.1007/s10546-005-9030-8.
- Parish, T. R., and K. T. Waight, 1987: The forcing of Antarctic katabatic winds. *Mon. Wea. Rev.*, **115**, 2214–2226, doi:10.1175/1520-0493(1987)115<2214:TFOAKW>2.0.CO;2.
- Peng, S., and J. S. Whitaker, 1999: Mechanisms determining the atmospheric response to midlatitude SST anomalies. *J. Climate*, **12**, 1393–1408, doi:10.1175/1520-0442(1999)012<1393:MDTART>2.0.CO;2.
- Perovich, D. K., and Coauthors, 1999: Year on ice gives climate insights. *Eos, Trans. Amer. Geophys. Union*, **80**, 481, 485–486, doi:10.1029/EO080i041p00481-01.
- Persson, P. O. G., 2012: Onset and end of the summer melt season over sea ice: Thermal structure and surface energy perspective from SHEBA. *Climate Dyn.*, **39**, 1349–1371, doi:10.1007/s00382-011-1196-9.
- , C. W. Fairall, E. L. Andreas, P. S. Guest, and D. K. Perovich, 2002: Measurements near the Atmospheric Surface Flux Group tower at SHEBA: Near-surface conditions and surface energy budget. *J. Geophys. Res.*, **107**, 8045, doi:10.1029/2000JC000705.
- Petoukhov, V., and V. A. Semenov, 2010: A link between reduced Barents–Kara sea ice and cold winter extremes over northern continents. *J. Geophys. Res.*, **115**, D21111, doi:10.1029/2009JD013568.
- Porter, D. F., J. J. Cassano, and M. C. Serreze, 2011: Analysis of the Arctic heat budget in WRF: A comparison with reanalyses and satellite observations. *J. Geophys. Res.*, **116**, D22108, doi:10.1029/2011JD016622.
- , —, and —, 2012: Local and large-scale atmospheric responses to reduced Arctic sea ice and ocean warming in the WRF model. *J. Geophys. Res.*, **117**, D11115, doi:10.1029/2011JD016969.
- Powers, J. G., K. W. Manning, D. H. Bromwich, J. J. Cassano, and A. M. Cayette, 2012: A decade of Antarctic science support through AMPS. *Bull. Amer. Meteor. Soc.*, **93**, 1699–1712, doi:10.1175/BAMS-D-11-00186.1.
- Rinke, A., W. Maslowski, K. Dethloff, and J. Clement, 2006: Influence of sea ice on the atmosphere: A study with an Arctic atmospheric regional climate model. *J. Geophys. Res.*, **111**, D16103, doi:10.1029/2005JD006957.
- Royer, J. F., S. Planton, and M. Déqué, 1990: A sensitivity experiment for the removal of Arctic sea ice with the French spectral general circulation model. *Climate Dyn.*, **5**, 1–17, doi:10.1007/BF00195850.
- Schweiger, A., R. Lindsay, J. Zhang, M. Steele, H. Stern, and R. Kwok, 2011: Uncertainty in modeled Arctic sea ice volume. *J. Geophys. Res.*, **116**, C00D06, doi:10.1029/2011JC007084.
- Screen, J. A., and I. Simmonds, 2010: The central role of diminishing sea ice in recent Arctic temperature amplification. *Nature*, **464**, 1334–1337, doi:10.1038/nature09051.
- , and —, 2013: Caution needed when linking weather extremes to amplified planetary waves. *Proc. Natl. Acad. Sci. USA*, **110**, E2327, doi:10.1073/pnas.1304867110.
- , —, and K. Keay, 2011: Dramatic interannual changes of perennial Arctic sea ice linked to abnormal summer storm activity. *J. Geophys. Res.*, **116**, D15105, doi:10.1029/2011JD015847.

- , C. Deser, and I. Simmonds, 2012: Local and remote controls on observed Arctic warming. *Geophys. Res. Lett.*, **39**, L10709, doi:10.1029/2012GL051598.
- , I. Simmonds, C. Deser, and R. Tomas, 2013: The atmospheric response to three decades of observed Arctic sea ice loss. *J. Climate*, **26**, 1230–1248, doi:10.1175/JCLI-D-12-00063.1.
- , C. Deser, I. Simmonds, and R. Tomas, 2014: Atmospheric impacts of Arctic sea-ice loss, 1979–2009: Separating forced change from atmospheric internal variability. *Climate Dyn.*, **43**, 333–344, doi:10.1007/s00382-013-1830-9.
- Seierstad, I. A., and J. Bader, 2009: Impact of a projected future Arctic sea ice reduction on extratropical storminess and the NAO. *Climate Dyn.*, **33**, 937–943, doi:10.1007/s00382-008-0463-x.
- Semmler, T., R. McGrath, and S. Wang, 2012: The impact of Arctic sea ice on the Arctic energy budget on the climate of the northern mid-latitudes. *Climate Dyn.*, **39**, 2675–2694, doi:10.1007/s00382-012-1353-9.
- Seo, H., and J. Yang, 2013: Dynamical response of the Arctic atmospheric boundary layer process to uncertainties in sea ice concentration. *J. Geophys. Res. Atmos.*, **118**, 12 383–12 402, doi:10.1002/2013JD020312.
- , Y.-O. Kwon, and J.-J. Park, 2014: On the effect of the East/Japan Sea SST variability on the North Pacific atmospheric circulation in a regional climate model. *J. Geophys. Res. Atmos.*, **119**, 418–444, doi:10.1002/2013JD020523.
- Serreze, M. C., and J. Francis, 2006: Arctic amplification. *Climatic Change*, **76**, 241–264, doi:10.1007/s10584-005-9017-y.
- , A. P. Barrett, A. G. Slater, M. Steele, J. Zhang, and K. E. Trenberth, 2007: The large-scale energy budget of the Arctic. *J. Geophys. Res.*, **112**, D11122, doi:10.1029/2006JD008230.
- , —, J. C. Stroeve, D. N. Kindig, and M. M. Holland, 2009: The emergence of surface-based Arctic amplification. *Cryosphere*, **3**, 11–19, doi:10.5194/tc-3-11-2009.
- Simmonds, I., 2015: Comparing and contrasting the behaviour of Arctic and Antarctic sea ice over the 35 year period 1979–2013. *Ann. Glaciol.*, **56**, 18–28, doi:10.3189/2015AoG69A909.
- , and W. F. Budd, 1991: Sensitivity of the Southern Hemisphere circulation to leads in the Antarctic pack ice. *Quart. J. Roy. Meteor. Soc.*, **117**, 1003–1024, doi:10.1002/qj.49711750107.
- , and X. Wu, 1993: Cyclone behaviour response to changes in winter Southern Hemisphere sea-ice zone. *Quart. J. Roy. Meteor. Soc.*, **119**, 1121–1148, doi:10.1002/qj.49711951313.
- , and P. D. Govekar, 2014: What are the physical links between Arctic sea ice loss and Eurasian winter climate? *Environ. Res. Lett.*, **9**, 101003, doi:10.1088/1748-9326/9/10/101003.
- Singarayer, J. S., J. L. Bamber, and P. J. Valdes, 2006: Twenty-first-century climate impacts from a declining Arctic sea ice cover. *J. Climate*, **19**, 1109–1125, doi:10.1175/JCLI3649.1.
- Skamarock, W. C., and Coauthors, 2008: A description of the Advanced Research WRF version 3. NCAR Tech. Note NCAR/TN-475+STR, 113 pp. [Available online at http://www.mmm.ucar.edu/wrf/users/docs/arw_v3_bw.pdf.]
- Stammerjohn, S. E., D. G. Martinson, R. C. Smith, X. Yuan, and D. Rind, 2008: Trends in Antarctic annual sea ice retreat and advance and their relation to El Niño–Southern Oscillation and Southern Annular Mode variability. *J. Geophys. Res.*, **108**, C03S90, doi:10.1029/2007JC004269.
- Steinhoff, D. F., D. H. Bromwich, and A. J. Monaghan, 2013: Dynamics of the foehn mechanism in the McMurdo Dry Valleys of Antarctica from Polar WRF. *Quart. J. Roy. Meteor. Soc.*, **139**, 1615–1631, doi:10.1002/qj.2038.
- Strey, S. T., W. L. Chapman, and J. E. Walsh, 2010: The 2007 sea ice minimum: Impacts on the Northern Hemisphere atmosphere in late autumn and early winter. *J. Geophys. Res.*, **115**, D23103, doi:10.1029/2009JD013294.
- Stroeve, J., M. M. Holland, W. Meier, T. Scambos, and M. Serreze, 2007: Arctic sea ice decline: Faster than forecast. *Geophys. Res. Lett.*, **34**, L09501, doi:10.1029/2007GL029703.
- , M. C. Serreze, M. M. Holland, J. E. Kay, J. Maslanik, and A. P. Barrett, 2012: The Arctic's rapidly shrinking sea ice cover: A research synthesis. *Climatic Change*, **110**, 1005–1027, doi:10.1007/s10584-011-0101-1.
- Sturm, M., D. K. Perovich, and J. Holmgren, 2002: Thermal conductivity and heat transfer through the snow on the ice of the Beaufort Sea. *J. Geophys. Res.*, **107**, 8043, doi:10.1029/2000JC000409.
- Tang, Q., X. Zhang, X. Yang, and J. A. Francis, 2013: Cold winter extremes in northern continents linked to Arctic sea ice loss. *Environ. Res. Lett.*, **8**, 014036, doi:10.1088/1748-9326/8/1/014036.
- Uttal, T., and Coauthors, 2002: Surface heat budget of the Arctic Ocean. *Bull. Amer. Meteor. Soc.*, **83**, 255–275, doi:10.1175/1520-0477(2002)083<0255:SHBOTA>2.3.CO;2.
- Vihma, T., 2014: Effects of Arctic sea ice decline on weather and climate: A review. *Surv. Geophys.*, **35**, 1175–1214, doi:10.1007/s10712-014-9284-0.
- Wang, W., and Coauthors, 2013: ARW: Version 3 modeling system user's guide. NCAR Tech. Note, 408 pp. [Available online at http://www2.mmm.ucar.edu/wrf/users/docs/user_guide_V3/ARWUsersGuideV3.pdf.]
- Warren, S. G., I. G. Rigor, N. Untersteiner, V. F. Radionov, N. N. Bryazgin, Y. I. Aleksandrov, and R. Colony, 1999: Snow depth on arctic sea ice. *J. Climate*, **12**, 1814–1829, doi:10.1175/1520-0442(1999)012<1814:SDOASI>2.0.CO;2.
- Wilson, A. B., D. H. Bromwich, and K. M. Hines, 2011: Evaluation of Polar WRF forecasts on the Arctic System Reanalysis domain: Surface and upper air analysis. *J. Geophys. Res.*, **116**, D11112, doi:10.1029/2010JD015013.
- , —, and —, 2012: Evaluation of Polar WRF forecasts on the Arctic System Reanalysis domain. 2. Atmospheric hydrologic cycle. *J. Geophys. Res.*, **17**, D04107, doi:10.1029/2011JD016765.
- Yang, S., and J. H. Christensen, 2012: Arctic sea ice reduction and European cold winters in CMIP5 climate change experiments. *Geophys. Res. Lett.*, **39**, L20707, doi:10.1029/2012GL053338.
- Zygmuntowska, M., P. Rampal, N. Ivanova, and L. H. Smedsrud, 2014: Uncertainties in Arctic sea ice thickness and volume: New estimates and implications for trends. *Cryosphere*, **8**, 705–720, doi:10.5194/tc-8-705-2014.